A review of Smart Dust architecture, dynamics, and mission applications

Lorenzo Niccolai, Marco Bassetto, Alessandro A. Quarta*, Giovanni Mengali

Department of Civil and Industrial Engineering, University of Pisa, I-56122, Italy

Abstract

A Smart Dust is a propellantless femtosatellite, with a characteristic side length of a few millimeters and a high value of its area-to-mass ratio. It exploits the solar radiation pressure to create a propulsive acceleration sufficient enough to substantially affect its orbital dynamics. A number of new mission concepts may thus be envisaged, where the Smart Dust is either used as a single spacecraft or, more often, within a swarm of objects that communicate and exchange information among them. This paper discusses the state of the art of the Smart Dust concept, which has received a major boost by the rise of small satellite market and by the new manufacturing technologies of miniaturized electric and mechanical components. After a general description of the basic architecture of a Smart Dust, this work concentrates on the analysis of its dynamics in both heliocentric and geocentric mission scenarios, and highlights the different available approaches. An overview of possible mission applications is presented, and potential future developments and technological challenges are investigated.

Keywords: Smart Dust, femtosatellite, electrochromic control system, solar sail

Nomenclature

$\mathbb{A}$, $\mathbb{B}$, $\mathbb{C}$	=	auxiliary matrices, see Eq. (24)
A	=	Smart Dust frontal area, $[\mathrm{m}^2]$
A_{drag}	=	area exposed to atmospheric drag, $[\mathrm{m}^2]$
A_{SRP}	=	illuminated area, $[\mathrm{m}^2]$
a	=	semimajor axis, [km]
a_r, a_θ	=	radial and circumferential propulsive acceleration, $[\mathrm{mm/s}^2]$
b_i	=	force coefficients
C	=	spacecraft center of mass
c_D	=	drag coefficient
c_r	=	reflection coefficient
$\mathbb{D}$, $\mathbb{E}$, $\mathbb{F}$	=	auxiliary matrices, see Eqs. (26)–(28)
E	=	Earth's center-of-mass
e	=	eccentricity
$H(z)$	=	Heaviside step function of variable z
h	=	Hamiltonian function
h_p	=	perigee altitude, [km]
i	=	generic working cycle
J_2	=	Earth's second-degree zonal harmonic
m	=	total Smart Dust mass, [kg]

*Corresponding author

Email addresses: lorenzo.niccolai@ing.unipi.it (Lorenzo Niccolai), marco.bassetto@ing.unipi.it (Marco Bassetto), a.quarta@ing.unipi.it (Alessandro A. Quarta), g.mengali@ing.unipi.it (Giovanni Mengali)

Published in Progress in Aerospace Sciences, Vol. 106 April 2019, pp. 1–14. doi: https://doi.org/10.1016/j.paerosci.2019.01.003

N = total number of working cycles
n = number of Smart Dusts in a given area, [km^{-2}]
$n_\oplus$ = Earth's orbital mean motion, [deg/year]
O = Sun's center-of-mass
$P_\oplus$ = solar radiation pressure, [Pa]
p = semilatus rectum, [km]
R = dimensionless radial propulsive acceleration
$R_\oplus$ = Earth's mean radius (6378 km)
r = primary body-spacecraft distance, [km]
$r_\oplus$ = Sun-Earth distance (1 au)
T = dimensionless circumferential propulsive acceleration
T_c = orbital period, [days]
t = time, [days]
t_{hl} = half-life degradation time, [days]
u, v = radial and circumferential component of velocity, [km/s]
$\boldsymbol{x}$ = state vector
$\boldsymbol{v}_{\mathrm{s/a}}$ = Smart Dust velocity w.r.t. the atmosphere (with $v_{\mathrm{s/a}} \triangleq \|\boldsymbol{v}_{\mathrm{s/a}}\|$), [km/s]
x = auxiliary variable, see Eqs. (7) and (10)
α = Sun incidence angle, [deg]
β = lightness number
γ = auxiliary parameter, see Eq. (44)
Δ = difference, variation
ϵ = degradation parameter, see Eq. (15)
θ = angular coordinate, [deg]
κ = J_2-related parameter, see Eq. (44)
λ = Smart Dust longitude, [deg]
$\lambda_\odot$ = Sun's true longitude, [deg]
$\mu_\odot$ = Sun's gravitational parameter, [$\mathrm{km}^3/\mathrm{s}^2$]
ρ = spacecraft-Smart Dust radial distance, [km]
ρ_a = atmospheric density, [kg/m^3]
τ = switching parameter
ϕ = Smart Dust-spacecraft angular separation, [deg]
$\dot{\bar{\phi}}_{\mathrm{des}}$ = design angular drift, [deg/year]
Ω = angular velocity, [deg/day]
ω = argument of perigee, [deg]

Subscripts

0 = initial
c = spacecraft circular orbit
drag = effect due to atmospheric drag
E = relative to the Earth
esc = escape condition
fin = final
grav = effect due to gravitational harmonics
J_2 = effect due to J_2
max = maximum
min = minimum
off = control system turned off
on = control system turned on
rel = relative
SRP = effect due to SRP

Superscripts

$\dot{}$ = time derivative
$'$ = derivative w.r.t. the polar angle θ
$\sim$ = dimensionless variable
$+$ = source term
$-$ = sink term

1. Introduction

Over the last century, the progress of space exploration has imposed demanding requirements on payloads and increased the spacecraft complexity, with the result of a constant rise in their average launch mass. To make a simple example, the Sputnik mass was 84 kg only, while a few scientific or remote-sensing satellites launched in the late 1990s or in the early 2000s outweighed 7000 kg [1, 2]. More recently, however, there has been a reversal in that trend, due to the dramatic growth of the small-sized spacecraft market, especially in the last two decades [3, 4]. Actually, space industries and agencies are currently more interested in satellites with launch masses below 10 kg, such as nanosatellites, picosatellites, and femtosatellites [5]. These spacecraft categories will now be collected and referred to with the name of Very Small Satellites (VSSs). A thorough classification of satellites with a mass less than 100 kg is shown in Tab. 1 [5]. VSSs are a very active and promising option for space missions, of which the strength is especially due to their significant cost reduction when compared to conventional spacecraft configurations. In fact, VSSs are much less expensive in terms of manufacturing costs, and may exploit the possibility of using commercial components for the production of various identical (or similar) spacecraft [6]. They are also economic in terms of launch costs, since one or more VSSs can be fitted in a single launcher either as a primary, or a secondary piggyback payload. The cost reduction guaranteed by VSSs has also dramatically increased the number of mission opportunities and opened the space access to small nations and even universities [5, 7, 8, 9, 10, 11]. An additional important advantage of VSSs, related to their possibility of deploying a number of satellites with a single launch, is that they guarantee an effective risk mitigation via redundancy, and give also the opportunity of planning special mission scenarios that would be otherwise unfeasible with a single "conventional" spacecraft. The

Table 1: Classification of small spacecraft based on their mass.

Satellite class	**Mass**
Microsatellite	$10 - 100\,\mathrm{kg}$
Nanosatellite	$1 - 10\,\mathrm{kg}$
Picosatellite	$0.1 - 1\,\mathrm{kg}$
Femtosatellite	$0.01 - 0.1\,\mathrm{kg}$

first nanosatellite capable of executing all the typical spacecraft in-orbit operations, including attitude and orbit determination and control, was SNAP-1 [12, 13, 14], whereas the first picosatellite, launched in space by students from Stanford University, was the Orbiting Picosatellite Activated Launcher (OPAL) [7]. The satellite miniaturization concept is still a relevant topic, which involves both nanosatellites and picosatellites in many recent space missions [15], with special emphasis on distributed satellite missions [16], as will be discussed in detail later on. A major boost to the rise of VSSs was due to the development of the CubeSat project by students from Cal Poly and Stanford universities [7, 17, 18]. A CubeSat is a standardized small satellite, whose mass of about 1 kg may be placed in the boundary region between picosatellites and nanosatellites, see Tab. 1. Its revolutionary feature is in its dramatic cost-lowering capability, due to the use of Commercial Off-The-Shelf (COTS) components [19, 20, 21] and standardized platforms, which enables the assembly of satellites made of multiple standard units, such as 3U, 6U, or 12U-CubeSats. The notable success of CubeSats is confirmed by the number of space missions in which they are either directly involved [22, 23] or planned to be used, both for technology demonstration purposes [9, 10] and for other space operations [24, 25, 26, 27].

Because CubeSats are made of different, yet suitably assembled parts, a further reduction of the spacecraft launch mass may be obtained by reducing the size of each component, and by integrating them in a more compact structure. The first goal can be achieved thanks to the progress of micro and nano-technology

that, starting from the end of the 1980s [28], enables the manufacture of very small electrical and mechanical components [29], including solar cells, processors, batteries, GPS receivers and sensors. A recent result of this miniaturization process is the design of integrated components called Micro-Electro-Mechanical Systems (MEMS), which pave the way for many possible space applications [30, 31]. The goal for an optimal structural arrangement is instead simplified by the Complementary-Metal-On-Silicon (CMOS) technology [32], which consists in integrating miniaturized components into a common substrate of silicon wafer layers. This arrangement gives the possibility of creating a single component-satellite, capable of generating and distributing power, exchanging heat with the environment, communicating, and hosting a payload. With such an idea in mind, Barnhart et al. [33, 34, 35] proposed the concept of Satellite-on-a-chip (or SpaceChip), that is, a femtosatellite with a mass of about 10 g, whose subsystems are assembled in a 20 mm × 20 mm × 3 mm monolithic integrated circuit, as is shown in Fig. 1.

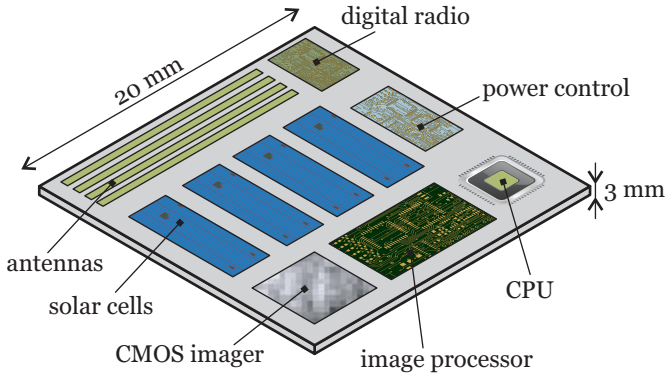

Figure 1: Schematic arrangement of a SpaceChip, adapted from Ref. [35].

More recently, Barnhart et al. [36, 37] presented the Satellite on a Printed Circuit Board (PCBSat) project, see Fig. 2. Unlike the SpaceChip, the latter is a "bottom-up" design approach, of which the main feature consists in using COTS components to reduce the manufacture costs and design complexity, but which results in a total mass greater than that of the SpaceChip. Other femtosatellite designs have been recently proposed and discussed, including WikiSat [38], based on COTS components, and SWIFT [39], which is equipped with a sensor and a small control system and is especially suited for swarm applications.

The remarkable success of femtosatellites is confirmed not only by an active research about their applications, but also by several operating missions, such as the first Peruvian space mission, started in 2013 [40], when the 1U-CubeSat PUCP-Sat deployed in orbit the 97 g-Pocket PUCP-Sat, which became the first orbiting femtosatellite. Another femtosatellite that has been already used for a space mission design is the Manchester's "Sprite" concept [41], see Fig. 3, which was financed through the crowd-funding website Kickstarter. Sprite was tested in 2011 with the MISSE-8 experiment on the International Space Station, with special emphasis on the communication system and on the reliability of the electrical components in the space environment. The promising outcomes of the test led in 2014 to the KickSat mission [41], when a 3U CubeSat was supposed to deploy a Sprite satellite in a LEO, but a failure due to a radiation event occurred and the deployment did not take place. However, a KickSat-2 has been already announced, and the recent space missions Max Valier Sat and Venta-1 [42] carry on six Sprites onboard.

A common peculiarity of all the proposed femtosatellite concepts is in their high value of area-to-mass ratio A/m, due to the characteristic length reduction [43] and the satellite shape, which resembles that of a thin, nearly rigid, plate. The values of A/m for the previously presented satellites are listed in Table 2, along with other design characteristics. The area-to-mass ratio is a fundamental parameter for describing how much the spacecraft dynamics is affected by pressure forces, such as the solar radiation pressure (SRP) or the atmospheric drag, and for quantifying its deviations from a purely Keplerian motion. High values of area-to-mass ratio make SpaceChips and other femtosatellites to be very sensible to orbital perturbations, a peculiarity that may be exploited to generate unique mission scenarios, otherwise unfeasible or very difficult to achieve with conventional spacecraft. In analogy with classical solar sails, the femtosatellite capability of exploiting the SRP to generate a propulsive acceleration is usually quantified through the lightness number

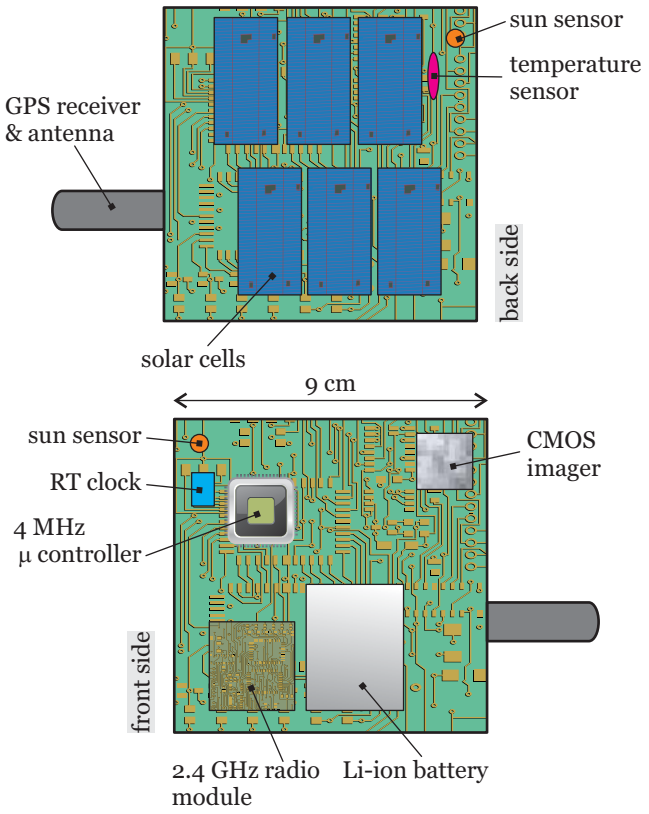

Figure 2: Front and back schematic views of PCBSat, adapted from Ref. [36].

β [44], which is a performance parameter defined as the ratio of the maximum acceleration due to SRP to the gravitational pull at a given heliocentric distance r. It is worth noting that, since these two effects both vary with the spacecraft distance from the Sun as r^{-2}, β is a constant (assuming the degradation of the reflective film to be neglected). An alternative performance parameter for a propellantless propulsive system is represented by its characteristic acceleration a_c [44], defined as the maximum propulsive acceleration that can be generated at a (reference) Sun-spacecraft distance equal to $r_\oplus \triangleq 1\,\text{au}$. The values of β and a_c for some femtosatellites are reported in Tab. 2.

Table 2: Characteristics of different femtosatellite designs, where A/m is the area-to-mass ratio, β is the lightness number, and a_c is the characteristic acceleration.

Satellite	A/m [m^2/kg]	β	a_c [mm/s^2]
SpaceChip	0.4	5.5×10^{-4}	3.3×10^{-3}
PCBSat	0.12	1.7×10^{-4}	10^{-3}
WikiSat	0.21	2.9×10^{-4}	1.7×10^{-3}
Pocket PUCP-Sat	0.042	5.9×10^{-5}	3.5×10^{-4}
SWIFT	0.016	2.2×10^{-5}	1.3×10^{-4}
Manchester's Sprite	0.245	5.5×10^{-4}	3.3×10^{-3}
Atchison's Sprite	17.391	0.0241	0.0105

The idea of manufacturing a femtosatellite capable of exploiting the SRP for new and exotic mission scenarios is at the heart of the Smart Dust (SD) design. In 1992, RAND Corporation conducted a workshop entitled "Future Technology-Driven Revolutions in Military Operations" where the germ of SD concept emerged. The first written traces of the "Smart Dust" term may be found in 1997, when Berlin and

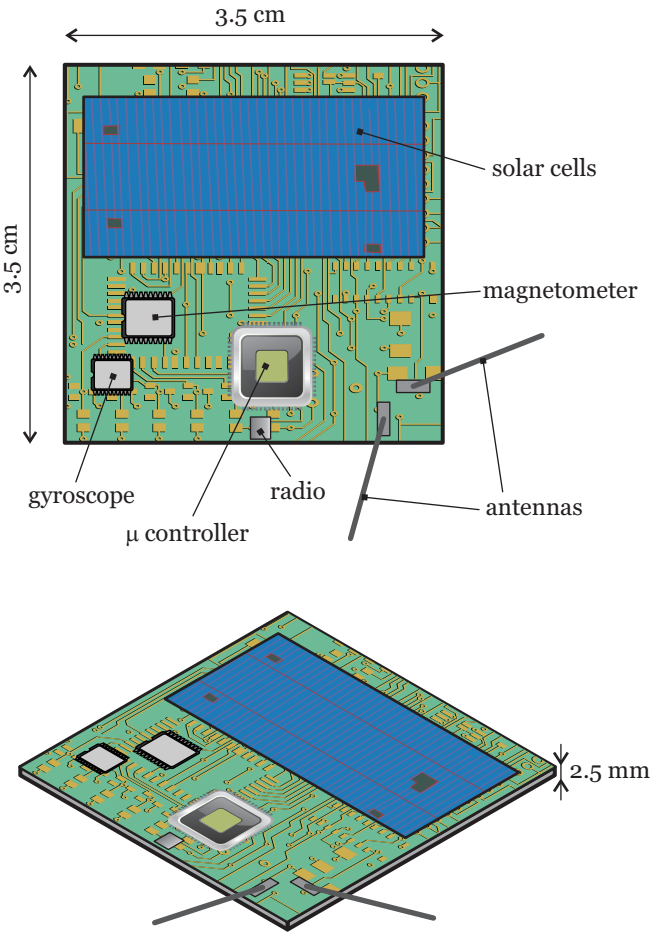

Figure 3: Sprite ChipSat, adapted from Ref. [41].

Gabriel [45] suggested the possibility of packing a sensor, a communication system and a computer into a single unit, having a cubic millimeter size, which could be embedded into a larger network, made of distributed wireless sensors. In the same year, Pister and co-workers presented a research proposal, called just "Smart Dust", with the aim of developing a new family of distributed sensor network systems. The first complete architecture of a SD was discussed by Kahn et al. [46] and Warneke et al. [47], and consisted of a payload (sensor), a power system (a solar cell and a battery), and an integrated circuit capable of acquiring, processing, and storing data, performing energy management and communicating with the external world, see Fig. 4.

The aim of this work is to provide a systematic review of the SD concept, with a special emphasis on its heliocentric and geocentric dynamics and on possible mission applications. The remainder of this paper is organized as follows: Section 2 briefly describes the basic architecture of a SD, while Section 3 discusses possible strategies that could be used for its attitude control. The dynamics of a SD is then presented in the case of both heliocentric and geocentric motion, and the main characteristics of this femtosatellite are then used to analyze potential and advanced mission scenarios.

2. Smart Dust basic architecture

The pioneering work of Warneke et al. [47] provides the main features of a SD to be used in a near-Earth scenario, which requires a low clock frequency of the processor necessary to minimize the required power, and a low bus voltage (of about $0.1\,\mathrm{V} - 0.3\,\mathrm{V}$) to avoid leakage currents. A critical design aspect

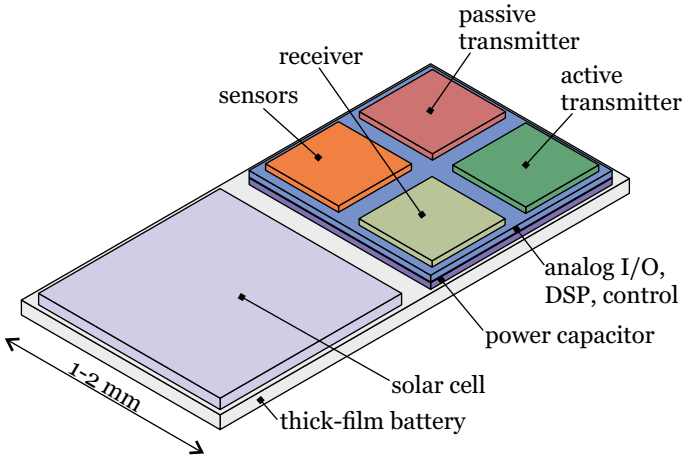

Figure 4: Schematic diagram of the smart dust concept proposed by Warneke et al. [47].

is to ensure a SD of an adequate communication capability, due to its low amount of available energy and its small size. To this end, some operations on acquired data must be performed by the processing unit, including thresholding, filtering, and spectral analysis, to reduce the data transmission volume. Antennas may communicate either through radio-frequency, when the technology level enables the manufacturing of micro-components, or through optical collimation, which exploits a wavelength smaller than radio waves to achieve an accurate pointing with a very small antenna. However, the latter strategy has a significant drawback, since it requires a very accurate pointing of the SD antenna towards the ground station [47], which considerably complicates the SD attitude control system design.

The requirements described in Ref. [47] have to be revised for specific mission scenarios, to suitably adapt the concept to in-orbit applications. In this work, the term SD will be used to refer to a femtosatellite with some specific features. More precisely, a SD is characterized by a maximum side length of a few centimeters and a very high area-to-mass ratio. As previously stated, a high area-to-mass ratio allows the SRP to be exploited as a propulsive force in a similar way as a solar sail is able to do. Indeed, a SD can be thought of as a very small solar sail-equipped spacecraft with all of the subsystems integrated on a thin plate. Pursuing such an idea, Atchison and Peck [48] proposed the design of a femtosatellite with the aim of testing the SRP propulsion. This concept may be considered as a sort of a SD precursor and, because the spacecraft of Ref. [48] is essentially a derivation of Manchester's Sprite satellite [41], it will be referred to as Atchison's Sprite in the rest of the work.

Atchison's Sprite structure is composed of ultra-thin layers of silicon deposed on a silicon-oxide substrate, which provides rigidity and handling capability during the fabrication process, but is then eventually removed, thus guaranteeing a final thickness of about 25 μm. A small width is an essential requirement to be met, since the propulsive acceleration generated by the SRP scales as the inverse of the thickness. The final result in terms of area-to-mass ratio and lightness number is very promising, as can be seen from Tab. 2. The spacecraft is nominally able of measuring the environmental temperature and calculating its instantaneous position with an onboard processing unit. The communication system is very simple, as it only consists of a beacon capable of transmitting a single beep at a single frequency, and its carrier is generated by a crystal oscillator and transmitted by a dipole antenna with a large beamwidth. The temperature data are transmitted by the carrier frequency, whereas the beep includes the orbital position data. The onboard power necessary for communication purposes amounts to 10 mW for a geocentric orbital altitude of about 500 km, but a very high gain antenna is required for the ground station. Power generation is obtained during the sunlight phase by a silicon-based solar cell (which is cheaper when compared to a Gallium-Arsenide substrate), whereas in eclipse conditions the spacecraft is powerless, due to the absence of a battery. It is remarkable that the proposed bus voltage amounts to 50 V, a value much larger than that of Ref. [47], the latter being imposed by the power storage requirements of the onboard capacitor that feeds the communication system. Such a high voltage is achievable with the current technology level. The thermal control is totally passive,

and exploits micro-radiators to avoid the formation of cracks where two different metals are in contact. A very important feature of Atchison's Sprite concept is in its capability of passively obtaining a Sun-pointing attitude, as it will be described in the next section.

3. Smart Dust control

Different strategies have been proposed for controlling the attitude of a femtosatellite. One of the first attempts was to use a "corner-cube" architecture, made of three mutually orthogonal plates [49, 50], which could theoretically be able to passively achieve a Sun-pointing attitude, see Fig. 5.

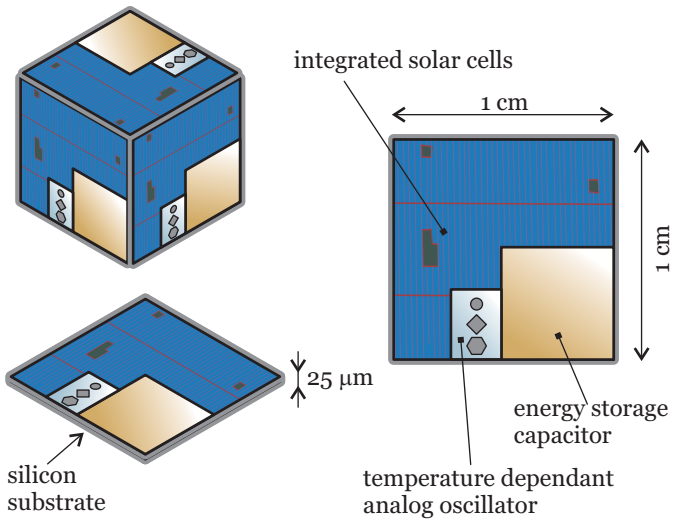

Figure 5: Passive sun-pointing corner-cube architecture, adapted from Ref. [48].

However, this configuration is not very effective because it decreases the lightness number and is also naturally unstable. Another possibility is to use a grated-plate femtosatellite [50], designed so as to obtain a displacement of the centre of pressure with respect to the (fixed) center of mass as a function of the pitch angle. Despite the existence of interesting preliminary results [50], this configuration has not been further investigated, probably because of the technical issues related to the manufacture of a grate on such a small object.

In 2010, Atchison and Peck [48] proposed a radically different design, composed of a single plate with many surface etches called "facets", which produce a torque dependent on their surface orientation and coating [51, 52]. This configuration exploits the secondary reflection effect, that is, the light reflected by a facet generates a pressure force by impinging on the neighbouring facets, see Fig. 6.

The hypothesized angles of the edges are 35 deg and 54 deg, measured with respect to the side walls. The inner walls are coated in such a way as to be absorptive, whereas the outer walls are reflective. Details about the fabrication process may be found in Ref. [48]. The facets are supposed to be strategically located on the spacecraft surface, so that the generated torque is a suitable function of the incidence angle α, that is, the angle between the Sun-spacecraft direction and the external normal to the SD surface. The resultant torque has a stabilizing effect, which induces the SD to passively maintain a Sun-facing configuration. The numerical simulations of Atchison's Sprite attitude dynamics report small oscillations of pitch and roll angles with a period of about 120 s [48].

A more complex control strategy involves the use of an Electrochromic Coating System (ECS). The latter exploits the well-known property of electrochromic materials of modifying their optical properties on application of a suitable electric voltage [53]. The idea of coating a solar sail with an ECS for attitude control purposes can be traced back to 1997 [54], and basically consists in varying the optical properties of the spacecraft surface to generate pitch and roll torques. This concept has been in-depth investigated by Wie [55], and has promoted some theoretical research on its potential mission applications [56, 57] and,

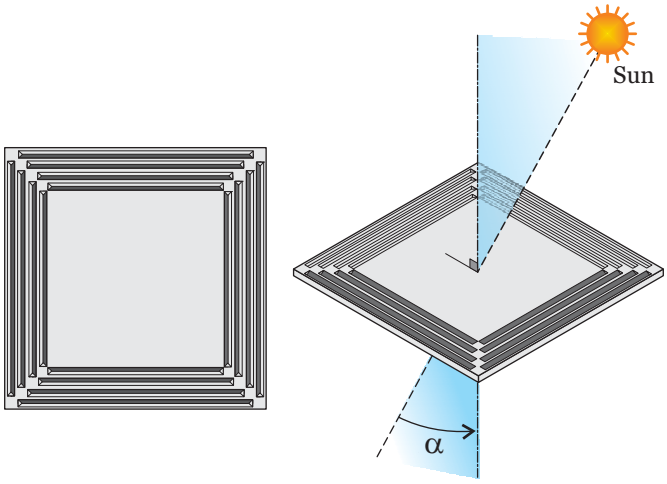

Figure 6: Schematic representation of a faceted surface, adapted from Ref. [48].

most importantly, has obtained an experimental verification [58, 59] through the first interplanetary solar sail mission, JAXA's IKAROS [60]. Figure 7 shows a schematic representation of IKAROS sail with the general arrangement of ECS for attitude control. The success of IKAROS attitude control system is a

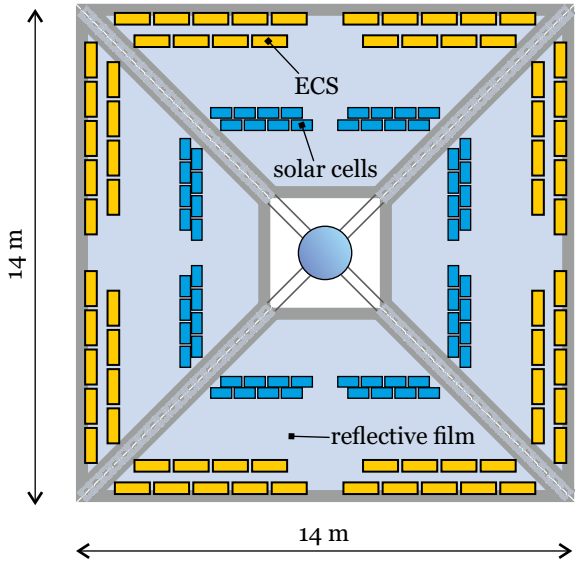

Figure 7: IKAROS solar sail scheme, adapted from Ref. [59].

promising starting point for a future implementation of an ECS on an SD satellite. Notably, an ECS could also be used not only to obtain control torques, but also to modulate the SD propulsive acceleration, as will be discussed in Section 4.

A different attitude control strategy consists in exploiting the so-called radiometric forces [61, 62, 63], which cause a variation of the drag coefficient as a function of the SD temperature. In essence, a spatial differentiation of the satellite temperature, generated by an onboard control system, may be used to get pitch and roll stabilizing torques. This strategy is especially interesting in geocentric mission applications, where the atmospheric drag is not negligible in a LEO. However, its practical implementation is made difficult by the presence of aerodynamic and magnetic torques [64].

The main drawback of all the previous attitude control systems is in their inability to produce a control

torque along the radial direction, which causes an unstable dynamics around the yaw axis. This issue may be overcome with the strategy proposed by Artusio-Glimpse and Swartzlander Jr. [65] and later extended to solar sail by Firuzi and Gong [66], who proposed the concept of providing the sail with refractive micro-prisms coated with Polymer Dispersed Liquid Crystals (PDLCs). The micro-prisms are used to refract the incident sunlight in such a way as to produce a tangential component of the propulsive acceleration even in a Sun-facing configuration. PLDCs are electrochromic materials of which the state may be changed from opaque to transparent upon applying an electric field [67], so that the refractive prisms are either activated (transparent state) or switched off (opaque state), see Fig. 8. In a SD design similar to that of Atchison's Sprite, a set of micro-prisms, suitably arranged with respect to the SD center of mass, may also generate a net yaw torque, as is shown in Fig. 9. This concept represents a significant improvement for SD design,

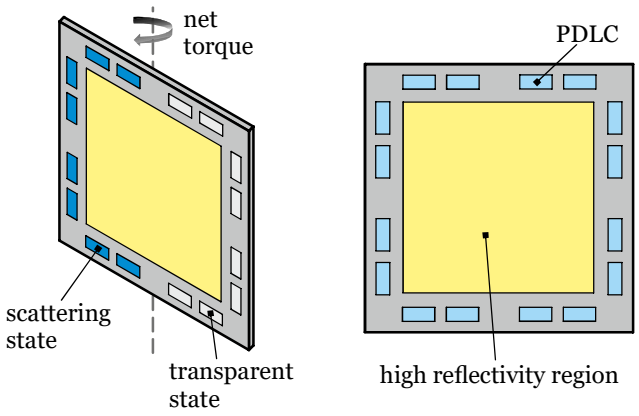

Figure 8: Conceptual scheme of attitude control with PDLC, adapted from Ref. [67].

because a single SD may be able to achieve a three-axis stabilization in a Sun-facing attitude without the need of heavy sensors or actuators.

4. Smart Dust heliocentric dynamics

The dynamics of a SD is usually described in the same way as that of orbital dust, that is, like celestial bodies with a characteristic length of less than $100\,\mu$m and a mass of a few micrograms [68]. The motion of these particles with a high area-to-mass ratio is largely influenced by surface forces, as observed in the Kuiper belt [69], and in the dust cloud released by a comet and eventually placed on a Solar System escape trajectory by the SRP force [70, 71].

There are two small, but long-acting forces that affect the motion of orbital dust. The first one is the Poynting-Robertson drag [72], caused by the different Doppler shift between forward and backward energy flux on an orbiting object, whereas the second one is the Yarkovsky effect [68], which is a force generated by the anisotropic emission of thermal photons on a rotating body. However, since the typical operative life of a spacecraft is much shorter than the dynamics of the Solar System, these two effects cause a very small perturbation on the SD dynamics, which is usually neglected. Such an assumption is in accordance with Ref. [48], and is confirmed by the results of Ref. [73]. In the remainder of this section, the SD heliocentric dynamics will thoroughly discussed from different viewpoints.

4.1. Inertial dynamics

The two-dimensional equations of motion of a SD propelled by the SRP force may be written in an inertial polar reference frame $\mathcal{T}_O\,(O; r, \theta)$, in which O is the Sun's center of mass, r is the Sun-SD distance

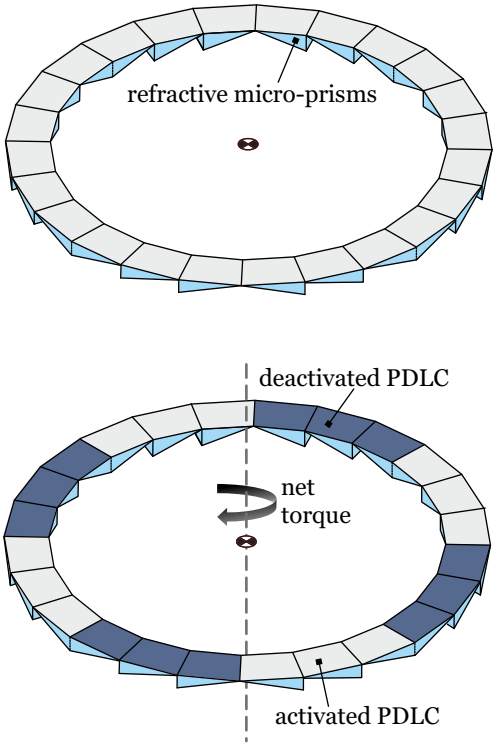

Figure 9: Conceptual scheme of yaw control with PDLC, adapted from Ref. [66].

and θ is an angular coordinate measured counterclockwise from a fixed direction, that is

$$\ddot{r} - r\,\dot{\theta}^2 = -\frac{\mu_\odot}{r^2}\,[1 - \beta\,R(\alpha)] \tag{1}$$

$$r\,\ddot{\theta} + 2\,\dot{r}\,\dot{\theta} = \beta\,\frac{\mu_\odot}{r^2}\,T(\alpha) \tag{2}$$

where the dot symbol denotes the time derivative, $\alpha \in [0,\, \pi/2]$ rad is the Sun incidence angle, while R and T are defined as [44, 74, 75]

$$R = \frac{b_1\,\cos\alpha + b_2\,\cos^3\alpha + b_3\,\cos^2\alpha}{b_1 + b_2 + b_3} \tag{3}$$

$$T = \frac{b_2\,\cos^2\alpha\sin\alpha + b_3\,\cos\alpha\sin\alpha}{b_1 + b_2 + b_3} \tag{4}$$

in which $\{b_1, b_2, b_3\}$ are the force coefficients [76], whose values depend on the thermo-optical characteristics of the reflective film. For example, using the data taken from Wright [77] and McInnes [44] (corresponding to a film with highly reflective aluminum coated front side and a highly emissive chromium-coated backside) the force coefficients are $b_1 = 0.0864$, $b_2 = 0.8272$, and $b_3 = -0.0055$. These data have been recently updated by Heaton and Artusio-Glimpse [75] to the new values $b_1 = 0.0723$, $b_2 = 0.8554$, and $b_3 = -0.0030$. In the ideal case of fully specular reflection of the impinging photons, the force coefficients are $b_1 = b_3 = 0$ and $b_2 = 1$. Figure 10 shows the dimensionless propulsive acceleration in the ideal case as a function of the incidence angle α.

Based on the above discussion, the motion of a SD in a heliocentric case is described assuming the spacecraft to be able to passively maintain a Sun-facing attitude. This objective may be achieved with one of the previously described strategies. Under such hypothesis, the dynamics is actually two-dimensional and,

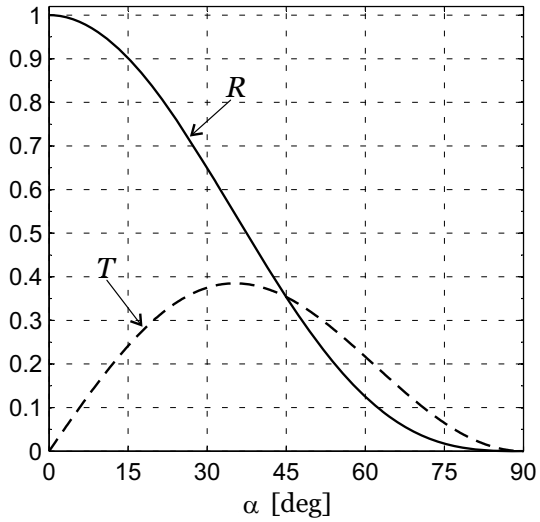

(a) Radial (R) and circumferential (T) dimensionless propulsive acceleration components, see Eqs. (3) and (4)

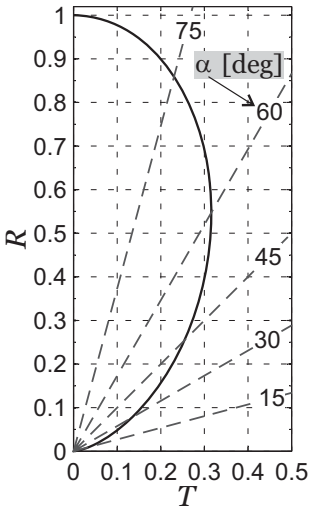

(b) Dimensionless propulsive acceleration $\sqrt{R^2+T^2}$ for different Sun incidence angles α

Figure 10: Dimensionless propulsive acceleration in case of specular reflection.

because $R(0) = 1$ and $T(0) = 0$, Eqs. (1)–(2) become

$$\ddot{r} - r\,\dot{\theta}^2 = -\frac{\mu_\odot}{r^2}\,(1-\beta) \tag{5}$$

$$\frac{\mathrm{d}}{\mathrm{d}t}\left(r^2\,\dot{\theta}\right) = 0 \tag{6}$$

Equation (6) states that the specific orbital angular momentum is a constant of motion, and so is the semilatus rectum p. Accordingly, Eq. (5) can be rewritten with a variable transformation proposed in Ref. [78], similar to that discussed by McInnes [79] and Yamakawa [80] for a classical solar sail, and by Quarta and Mengali [81] for an electric solar wind sail. The dimensionless auxiliary variable x is defined as

$$x \triangleq 1 - \beta - \frac{p_0}{r} \tag{7}$$

where the subscript 0 denotes the initial time instant $t_0 \triangleq 0$. Using the polar angle θ as the independent variable, Eq. (5) becomes

$$x'' + x = 0 \tag{8}$$

where the prime symbol represents a derivative taken with respect to θ. Since Eq. (8) is in the form of a harmonic oscillator, it can be easily integrated, thus obtaining an analytical expression of the Sun-SD distance as a function of the polar angle for a given lightness number β, viz.

$$r(\theta) = \frac{p_0}{1 - \beta - x_0\,\cos\theta - x_0'\,\sin\theta} \tag{9}$$

In a more general situation, the lightness number may be used as a control parameter. This is possible, as suggested by Mengali et al. [78], by coating the SD external surface with electrochromic material. Assuming the optical properties of the electrochromic material may be changed between two states, the lightness number takes two possible values, that is, $\beta_{\min}$ or $\beta_{\max} \triangleq \beta_{\min} + \Delta\beta$. To account for the ECS in the thrust model, a switching parameter $\tau \in \{0, 1\}$ is introduced, so that $\tau = 1$ and $\beta = \beta_{\max}$ when the ECS is switched on, otherwise $\tau = 0$ and $\beta = \beta_{\min}$ when it is switched off. A new expression for x is now introduced as

$$x \triangleq 1 - \beta_{\min} - \frac{p_0}{r} \tag{10}$$

and Eq. (8) becomes

$$x'' + x = \tau\,\Delta\beta \tag{11}$$

The analytical solution of Eq. (11) is [78]

$$x(\theta) = x_0\,\cos\theta + x'_0\,\sin\theta + \tau(\theta)\,\Delta\beta \tag{12}$$

with

$$\tau(\theta) = \sum_{i=1}^{N}\{H(\theta-\theta_{\mathrm{on}_i})[1-\cos(\theta-\theta_{\mathrm{on}_i})] - H(\theta-\theta_{\mathrm{off}_i})[1-\cos(\theta-\theta_{\mathrm{off}_i})]\} \tag{13}$$

where N is the total number of working cycles (each cycle starts when the ECS is switched on and ends when it is switched off), $H(z)$ is the Heaviside step function of the variable z, and θ_{on_i} (or θ_{off_i}) represents the polar angle at which the ECS is switched on (or off). The polar equation of a SD with ECS is

$$r(\theta) = \frac{p_0}{1-\beta_{\min}-x(\theta)} \tag{14}$$

with $x(\theta)$ given by Eq. (12). Note that Eqs. (9) and (14) can be seen as a modified version of the classical (Keplerian) polar equation. Equations (11)–(14) can be specialized to some particular cases, including a single working cycle ($N = 1$) or a periodic switching on/off of the ECS ($\theta_{\mathrm{on}_i} - \theta_{\mathrm{off}_i} = \Delta\theta$ for each value of i). More details may be found in Ref. [78].

4.2. Inertial dynamics with film degradation

A realistic study on SD dynamics must take into account the degradation of the reflecting film. This effect has been reported for a classical solar sail case [82, 83, 84] and may also occur for SD coatings. Mengali and Quarta [78] used the approach discussed in Ref. [85], assuming an exponential degradation of the optical properties. A degradation parameter ϵ is defined as

$$\epsilon \triangleq \frac{\ln(2)\,r_\oplus^2}{t_{\mathrm{hl}}\sqrt{\mu_\odot\,p_0}} \tag{15}$$

where $r_\oplus \triangleq 1\,\mathrm{au}$ is the Sun-Earth distance, and t_{hl} is the half-life degradation time. The latter is the time required by the optical reflectivity to reach the mean value between the beginning- and the end-of-life, which can be experimentally estimated. Using Eq. (15), Eq. (11) becomes

$$x'' + x = \tau\,\Delta\beta\,\exp(-\epsilon\,\theta) \tag{16}$$

and its solution for an ECS always switched on ($\tau \equiv 1$) is

$$r(\theta) = \frac{p_0}{1-\beta_{\min}-\left(x_0-\dfrac{\Delta\beta}{1+\epsilon^2}\right)\cos\theta-\left(x'_0+\dfrac{\epsilon\,\Delta\beta}{1+\epsilon^2}\right)-\dfrac{\Delta\beta}{1+\epsilon^2}\,\exp(-\epsilon\,\theta)} \tag{17}$$

which, for a large value of θ (when the exponential term becomes negligible), tends again to a conic. The general solution of Eq. (16), which accounts for N working cycles of the ECS, is more involved and may be found in Ref. [78].

4.3. Relative motion

The two-dimensional motion of a SD can also be investigated from a different point of view, by studying its heliocentric dynamics with respect to a given reference orbit, see Ref. [86]. This approach is especially useful for mission cases in which one or more SDs are released by a mother spacecraft (MS). The problem is mathematically tractable as long as the SD is sufficiently close to the MS, which moves along a reference circular orbit, with an orbital radius r_c and an angular velocity $\Omega_c = \sqrt{\mu_\odot/r_c^3}$. Assuming a Sun-facing

attitude of the SD, its heliocentric motion can be analyzed in a moving reference frame $\mathcal{T}_C\,(C;\rho,\phi)$, centered at the MS barycenter C and illustrated in Fig. 11, with the following equations [79]

$$\dot{\rho} = u_{\rm rel} \tag{18}$$

$$\dot{\phi} = \frac{v_{\rm rel}}{r_c} \tag{19}$$

$$\dot{u}_{\rm rel} = 2\,\Omega_c\,v_{\rm rel} + 3\,\Omega_c^2\,\rho + (\beta_{\min} + \tau\,\Delta\beta)\,\frac{\mu_\odot}{r_c^2} \tag{20}$$

$$\dot{v}_{\rm rel} = -2\,\Omega_c\,u_{\rm rel} \tag{21}$$

where ρ is the difference between the Sun-SD distance and the Sun-MS distance (with $|\rho| \ll r_c$), ϕ is the SD-MS angular separation, and $u_{\rm rel}$ (or $v_{\rm rel}$) is the radial (or circumferential) relative velocity of the SD with respect to the MS. Since by assumption the propulsive acceleration is always along the radial direction,

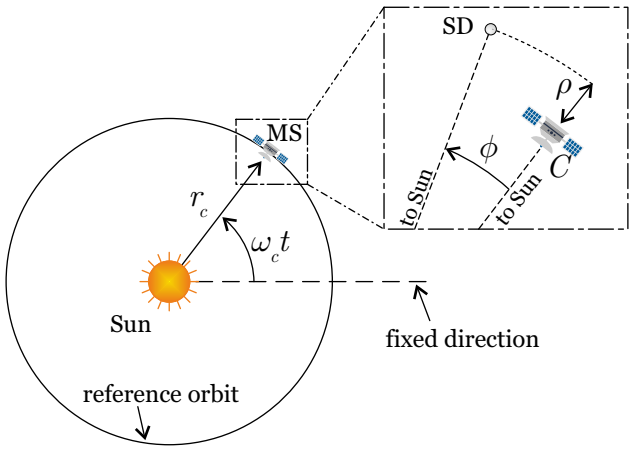

Figure 11: Reference frame for the SD relative motion.

the only control variable is τ, which may be written as a function of the flight time t as

$$\tau(t) = \sum_{i=1}^{N} H(t - t_{{\rm on}_i}) - \sum_{i=1}^{N} H(t - t_{{\rm off}_i}) \tag{22}$$

where $t_{{\rm on}_i}$ (or $t_{{\rm off}_i}$) denotes the time instant at which the ECS is switched on (or off). Equations (18)–(21) can be conveniently rewritten in matrix form, viz.

$$\dot{\boldsymbol{x}} = \mathbb{A}\,\boldsymbol{x} + \tau\,\mathbb{B} + \mathbb{C} \tag{23}$$

where $\boldsymbol{x} \triangleq [\rho,\ \phi,\ u_{\rm rel},\ v_{\rm rel}]^T$ is the state vector, whereas the matrices $\mathbb{A}$, $\mathbb{B}$ and $\mathbb{C}$ are defined as

$$\mathbb{A} \triangleq \begin{bmatrix} 0 & 0 & 1 & 0 \\ 0 & 0 & 0 & 1/r_c \\ 3\,\Omega_c^2 & 0 & 0 & 2\,\Omega_c \\ 0 & 0 & -2\,\Omega_c & 0 \end{bmatrix} \quad , \quad \mathbb{B} \triangleq \begin{bmatrix} 0 \\ 0 \\ \Delta\beta\,r_c\,\Omega_c^2 \\ 0 \end{bmatrix} \quad , \quad \mathbb{C} \triangleq \begin{bmatrix} 0 \\ 0 \\ \beta_{\min}\,r_c\,\Omega_c^2 \\ 0 \end{bmatrix} \tag{24}$$

The solution of Eq. (23) is [86]

$$\boldsymbol{x}(t) = \mathbb{D}(t)\,\boldsymbol{x}_0 + \mathbb{E}(t) + \Delta\beta \sum_{i=1}^{N} \{H(t - t_{{\rm on}_i})\,\mathbb{F}(t, t_{{\rm on}_i}) - H(t - t_{{\rm off}_i})\,\mathbb{F}(t, t_{{\rm off}_i})\} \tag{25}$$

where $\boldsymbol{x}_0$ is the state vector at $t = t_0$, and

$$\mathbb{D}(t) \triangleq \begin{bmatrix} 4 - 3\,\cos(\Omega_c\,t) & 0 & \dfrac{\sin(\Omega_c\,t)}{\Omega_c} & \dfrac{2\,[1-\cos(\Omega_c\,t)]}{\Omega_c} \\ \dfrac{6[\sin(\Omega_c\,t) - \Omega_c\,t]}{r_c} & 1 & \dfrac{2\,[\cos(\Omega_c\,t) - 1]}{\Omega_c\,r_c} & \dfrac{4\,\sin(\Omega_c\,t) - 3\,\Omega_c\,t}{\Omega_c\,r_c} \\ 3\,\Omega_c\,\sin(\Omega_c\,t) & 0 & \cos(\Omega_c\,t) & 2\,\sin(\Omega_c\,t) \\ 6\,\Omega_c[\cos(\Omega_c\,t) - 1] & 0 & -2\,\sin(\Omega_c\,t) & 4\,\cos(\Omega_c\,t) - 3 \end{bmatrix} \tag{26}$$

$$\mathbb{E}(t) \triangleq \beta_{\min} \begin{bmatrix} r_c\,[1 - \cos(\Omega_c\,t)] \\ 2\,[\sin(\Omega_c\,t) - \Omega_c\,t] \\ \Omega_c\,r_c\,\sin(\Omega_c\,t) \\ 2\,\Omega_c\,r_c\,[\cos(\Omega_c\,t) - 1] \end{bmatrix} \tag{27}$$

$$\mathbb{F}(t,z) \triangleq \begin{bmatrix} r_c\,[1 - \cos(\Omega_c\,t - \Omega_c\,z)] \\ 2\,[\sin(\Omega_c\,t - \Omega_c\,z) - \Omega_c\,t + \Omega_c\,z] \\ \Omega_c\,r_c\sin(\Omega_c\,t - \Omega_c\,z) \\ 2\,\Omega_c\,r_c\,[\cos(\Omega_c\,t - \Omega_c\,z) - 1] \end{bmatrix} \tag{28}$$

The time variation of ρ can be taken out from Eq. (25). As a result, its magnitude does not exceed un upper limit, that is

$$|\rho|\,/r_c \leq 7\,|\rho_0|\,/r_c + 2\,\beta_{\min} + \frac{4\,|u_{\mathrm{rel}_0}| + |v_{\mathrm{rel}_0}|}{\Omega_c\,r_c} + \Delta\beta\,(4\,N + 1) \tag{29}$$

Mengali et al. [86] investigated a special case, when the SD is deployed at t_0 with zero relative velocity with respect to the MS and $\Delta\beta = 0$. The latter condition models a failure of the ECS (i.e., $\beta \equiv \beta_{\min}$). Accordingly, Eq. (29) becomes

$$\rho_{\max} = 2\,\beta_{\min}\,r_c \tag{30}$$

and the time history of the angular coordinate ϕ is

$$\phi(t) = 2\,\beta_{\min}\,[\sin(\Omega_c\,t) - \Omega_c\,t] \tag{31}$$

Notably, when $\Delta\beta = 0$ and $\boldsymbol{x}_0 = 0$, it is found that $\rho(T_c) = 0$ and $u_{\mathrm{rel}}(T_c) = v_{\mathrm{rel}}(T_c) = 0$, where $T_c \triangleq 2\pi/\Omega_c$ is the MS orbital period. This implies that the SD returns on the reference orbit with zero relative velocity after one complete revolution of the MS, but with a different angular coordinate with respect to the MS, thus following an in-orbit phasing trajectory. The corresponding angular drift is

$$\Delta\phi = \phi(T_c) = -4\,\pi\,\beta_{\min} \tag{32}$$

Equations (30)–(32) may also be used in the case of SD without an ECS, by simply substituting $\beta_{\min}$ with the (unique) value of the lightness number β.

4.4. Continuum model

An alternative approach for studying the two-dimensional heliocentric dynamics of SDs consists in studying the motion of a large number of identical devices rather than that of a single femtosatellite. This amounts to describing the SDs with a continuum model, as proposed by McInnes [87]. Of course, this model is reasonable only provided a very large number of SDs is considered. This choice represents a very interesting option for SD missions, as will now be discussed. The analysis performed by McInnes [87] starts from the definition of a set of dimensionless polar variables, that is

$$\widetilde{r} \triangleq \frac{r}{r_0} \quad , \quad \widetilde{t} \triangleq t\,\sqrt{\frac{\mu_\odot\,(1-\beta)}{r_0^3}} \quad , \quad \widetilde{u} \triangleq \frac{u}{\sqrt{\mu_\odot/r_0}} \quad , \quad \widetilde{v} \triangleq \frac{v}{\sqrt{\mu_\odot/r_0}} \tag{33}$$

where u (or v) denotes the radial (or circumferential) component of the SD orbital velocity with respect to a heliocentric inertial reference frame, such as $\mathcal{T}_O$. The control volume is given by an annulus in the radial

interval $[\widetilde{r},\, \widetilde{r}+\mathrm{d}\widetilde{r}]$. If a number density n is defined as the number of devices in a given area, the continuity equation describing the evolution of n as a function of $\widetilde{r}$ and $\widetilde{t}$ may be written as

$$\frac{\partial n(\widetilde{r},\theta,\widetilde{t})}{\partial \widetilde{t}} + \frac{1}{\widetilde{r}}\frac{\partial}{\partial \widetilde{r}}\left[\widetilde{r}\,\widetilde{u}(\widetilde{r})\,n(\widetilde{r},\theta,\widetilde{t})\right] + \frac{1}{\widetilde{r}}\frac{\partial}{\partial \theta}\left[\widetilde{v}(\widetilde{r})\,n(\widetilde{r},\theta,\widetilde{t})\right] = \dot{n}^{+}(\widetilde{r},\theta,\widetilde{t}) - \dot{n}^{-}(\widetilde{r},\theta,\widetilde{t}) \tag{34}$$

where $\dot{n}^{+}$ (or $\dot{n}^{-}$) denotes the source (or sink) term, corresponding to a deposition rate (or a failure rate). Equation (34) is conveniently rewritten using the method of characteristics as

$$\frac{\mathrm{d}\widetilde{r}}{\mathrm{d}\widetilde{t}} = \widetilde{u}(\widetilde{r}) \tag{35}$$

$$\frac{\mathrm{d}\theta}{\mathrm{d}\widetilde{t}} = \frac{1}{\widetilde{r}}\,\widetilde{v}(\widetilde{r}) \tag{36}$$

$$\frac{\mathrm{d}n\,(\widetilde{r},\theta,\widetilde{t})}{\mathrm{d}\widetilde{r}} + n\,(\widetilde{r},\theta,\widetilde{t})\,\left[\frac{1}{\widetilde{r}} + \frac{1}{\widetilde{u}\,(\widetilde{r})}\,\frac{\mathrm{d}\widetilde{u}\,(\widetilde{r})}{\mathrm{d}\widetilde{r}}\right] = \frac{1}{\widetilde{u}\,(\widetilde{r})}\left[\dot{n}^{+}(\widetilde{r},\theta,\widetilde{t}) - \dot{n}^{-}(\widetilde{r},\theta,\widetilde{t})\right] \tag{37}$$

The expression of $\widetilde{r}(\widetilde{t})$ and $\theta(\widetilde{t})$ were derived in Ref. [88] under the hypothesis of quasi-circular SD orbit and fixed attitude. These two assumptions imply that a variation of the radial coordinate $\widetilde{r}$ can be obtained only by generating a circumferential component of the thrust, which excludes the use of a Sun-facing attitude. Indeed, in Ref. [88] the assumption is that each SD is capable of maintaining a fixed (non-Sun-facing) attitude, which may be obtained using the facets on the SD coating proposed by Atchison and Peck [48]. Different initial conditions have been simulated, considering both a constant deposition or a given failure rate, and several analytical solutions describing the time variation of the swarm dynamics have been obtained. This approach is interesting for future investigations on SD swarm mission scenarios, but some issues need to be addressed. In particular, the possibility of passively maintaining a fixed and non-Sun-facing attitude for a SD should be better investigated, since Atchison and Peck [48] only assessed the use of facets for a Sun-facing configuration. The minimum number of SDs necessary for applying the continuum model should also be quantified.

5. Smart Dust Geocentric dynamics

The dynamics of a SD in a geocentric context is rather different from the heliocentric case described in the previous section. The Eqs. (1)–(2) have first to be expressed in a suitable geocentric reference frame $\mathcal{T}_E\,(E; r_E, \theta_E)$, with origin in the Earth's center of mass E. The polar coordinates r and θ are now substituted with the Earth-spacecraft distance r_E and the (geocentric) polar angle θ_E, measured counterclockwise from a generic fixed direction. Also, for a SD orbiting around the Earth, the variation of the propulsive acceleration with the heliocentric distance r can be neglected by assuming $r \simeq r_{\oplus}$, while other effects, which are absent in a heliocentric scenario, become significant. In fact, in this case the orbital parameters of a SD are affected by the atmospheric drag, the Earth's flattening, and its shadow. Moreover, if the previously described facets are used to maintain a Sun-facing attitude, the propulsive acceleration does not act radially with respect to the primary (i.e., the Earth) and is a function of the SD attitude.

Colombo and McInnes [89, 90, 91] used a semi-analytical theory to compute the evolution of the SD orbital parameters under the influence of SRP, atmospheric drag, and Earth oblateness, with the assumption that the SD orbital plane coincides with the ecliptic one. Initially, they neglected the J_2 effect [89], which was instead taken into account in later works [90, 91]. The acceleration due to the SRP can be written in the frame $\mathcal{T}_E$ as

$$a_{r_E} = \frac{c_r\, P_{\oplus}\, A_{\mathrm{SRP}}}{m}\,\cos(\lambda+\nu) \quad , \quad a_{\theta_E} = -\frac{c_r\, P_{\oplus}\, A_{\mathrm{SRP}}}{m}\,\sin(\lambda+\nu) \tag{38}$$

where c_r is the reflectivity coefficient, $P_{\oplus} \simeq 4.56 \times 10^{-6}\,\mathrm{N/m^2}$ is the SRP at one astronomical unit, A_{SRP} is the area exposed to the Sun, and m is total SD mass. Finally, $(\lambda+\nu)$ refers to the angle, ranging in the interval $[0,\, 2\pi]$, between the Earth-SD vector and the Sun line. In particular, λ is the angle between the eccentricity vector and the Sun line, while ν is the SD true anomaly, see Fig. 12.

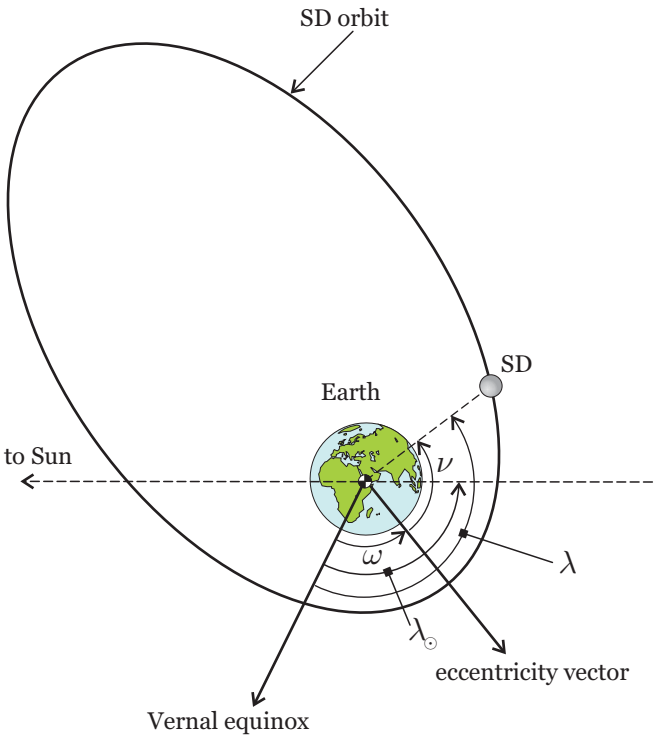

Figure 12: Sketch of a generic geocentric orbit scenario for SDs.

The analyses of Colombo and McInnes assume a SD to passively maintain a Sun-facing attitude, i.e., $A_{\mathrm{SRP}} \equiv A$. The magnitude of the propulsive acceleration is obtained as a function of β as

$$\|\boldsymbol{a}_p\| \triangleq \sqrt{a_{r_E}^2 + a_{\theta_E}^2} = \beta \, \frac{\mu_\odot}{r_\oplus^2} \tag{39}$$

The acceleration due to the atmospheric drag is given by

$$\boldsymbol{a}_{\mathrm{drag}} = -\frac{1}{2} \, \frac{c_D \, A_{\mathrm{drag}}}{m} \, \rho_{\mathrm{a}} \, v_{\mathrm{s/a}} \, \boldsymbol{v}_{\mathrm{s/a}} \tag{40}$$

where c_D is the drag coefficient, A_{drag} is the effective cross-sectional area of the SD, ρ_{a} is the atmospheric density, and $\boldsymbol{v}_{\mathrm{s/a}}$ is the SD velocity relative to the atmosphere, with $v_{\mathrm{s/a}} \triangleq ||\boldsymbol{v}_{\mathrm{s/a}}||$. In Refs. [89, 90, 91], the secular variation of the orbital parameters is obtained for each perturbation effect by averaging the Gauss' planetary equations. Then, the total secular variation of the Keplerian elements is expressed as the sum of each contribution, as is shown in the following equations

$$\Delta a \triangleq \Delta a_{\mathrm{SRP}} + \Delta a_{\mathrm{drag}} \quad , \quad \Delta e \triangleq \Delta e_{\mathrm{SRP}} + \Delta e_{\mathrm{drag}} \quad , \quad \Delta \omega \triangleq \Delta \omega_{\mathrm{SRP}} + \Delta \omega_{J_2} \tag{41}$$

where $\Delta\square_*$ denotes the variation of $\square$ due to $*$ in one orbital period. In particular, by neglecting the atmospheric rotation (i.e., assuming the angular velocity of the Earth to be zero), the secular variation of the argument of perigee due to drag is zero. The secular variation of the semimajor axis and the eccentricity due to J_2 is also null. Reference [91] discusses an algorithm for long-term orbit control based on changing the reflectivity coefficient of the SD through electrochromic control.

A thorough analysis of the long-term dynamics of SD geocentric trajectories is due to Zhao et al. [92], who refined the previous works by Colombo and McInnes [89, 90, 91] by modeling the SRP force, the atmospheric drag and Earth's sectorial gravitational harmonics up to degree two and order two. Similar to the previous works, their main assumptions [92] are that the atmosphere rotation and the Earth's axis tilt are both neglected, the SD orbit lies on the ecliptic plane, and the SD maintains a Sun-facing attitude.

The perturbation terms due to conservative forces are calculated by means of Lagrange's equations using a suitable perturbed potential function, whereas the effects of non-conservative forces are estimated with Gauss' equations. A mean variation of the orbital parameters in one revolution is obtained for the SRP term, which also includes the Earth's (cylindrical) shadow in the model. The complete expressions of $\mathrm{d}a/\mathrm{d}t$, $\mathrm{d}e/\mathrm{d}t$ and $\mathrm{d}\omega/\mathrm{d}t$ are here omitted for the sake of conciseness, but may be found in Ref. [92]. When these expressions for the time derivatives are integrated, the result is

$$\Delta a \triangleq \Delta a_{\mathrm{SRP}} + \Delta a_{\mathrm{drag}} \quad , \quad \Delta e \triangleq \Delta e_{\mathrm{SRP}} + \Delta e_{\mathrm{drag}} \quad , \quad \Delta\omega \triangleq \Delta\omega_{\mathrm{SRP}} + \Delta\omega_{\mathrm{grav}} \tag{42}$$

where the subscript "grav" accounts for all the zonal, tesseral, and sectorial gravitational harmonics, which affect the time history of the argument of perigee only. Equations (42) may be seen as the generalization of Eqs. (41). Due to its completeness, the model of Zhao et al. will be used to discuss the geocentric dynamics in Section 6. However, other approaches are presented in the remainder of this section, to give a complete overview of the different methods available for describing the SD geocentric motion.

An energetic method for the analysis of the two-body dynamics of a SD perturbed by the Earth oblateness and the SRP force is proposed in Refs. [93, 94]. Assuming the SD orbit to lie in the ecliptic plane, the dynamics in the $e-\lambda$ phase space form a Hamiltonian system, and the Hamiltonian expression of the orbit evolution due to the SRP and the J_2 perturbation is

$$h = -\sqrt{1-e^2} + \gamma\, e\, \cos\lambda - \frac{\kappa}{3\,(1-e^2)^{3/2}} \tag{43}$$

Equation (43) describes the SD trajectory in the $e-\lambda$ phase space, without taking into account the eclipses and the tilt of the Earth's axis with respect to the ecliptic plane. In Eq. (43), γ is related to the SRP force, while κ to the J_2 effect, that is

$$\gamma = \frac{3}{2}\sqrt{\frac{a}{\mu_\oplus}}\,\frac{c_r\,P_\oplus\,A_{\mathrm{SRP}}}{m\,n_\oplus} \quad , \quad \kappa = \frac{3}{2}\sqrt{\frac{\mu_\oplus}{a^7}}\,\frac{J_2\,R_\oplus^2}{n_\oplus} \tag{44}$$

where a is the orbital semimajor axis, $n_\oplus$ is the Earth's mean motion around the Sun, $R_\oplus$ is the Earth's radius, and J_2 is Earth's second-degree zonal harmonic. The secular rate of change of e and λ with respect to the true longitude of the Sun $\lambda_\odot$ (that is, the angle between the Sun line and the vernal equinox) is

$$\frac{\mathrm{d}e}{\mathrm{d}\lambda_\odot} = -\gamma\,\sin\lambda\,\sqrt{1-e^2} \quad , \quad \frac{\mathrm{d}\lambda}{\mathrm{d}\lambda_\odot} = -\gamma\,\cos\lambda\,\frac{\sqrt{1-e^2}}{e} + \frac{\kappa}{(1-e^2)^2} - 1 \tag{45}$$

The Hamiltonian expression in Eq. (43) has three stationary points [95], which are obtained by enforcing the necessary conditions

$$\frac{\mathrm{d}e}{\mathrm{d}\lambda_\odot} = 0 \quad , \quad \frac{\mathrm{d}\lambda}{\mathrm{d}\lambda_\odot} = 0 \tag{46}$$

Two of them, that is, $\{e,\,\lambda\} = \{0,\,0\}$ and $\{e,\,\lambda\} = \{0,\,\pi\}$, are stable. The third one is a hyperbolic equilibrium point located at $\{e,\,\lambda\} = \{e_h,\,\pi\}$, with $e_h \neq 0$. However, the actual existence of these three stationary points and the corresponding orbital eccentricities depend on γ and κ, that is, on the semimajor axis a and the area-to-mass ratio A_{SRP}/m [95]. In Ref. [96] the Hamiltonian expression of the orbit evolution is simplified by taking into account the perturbation due to the Earth's oblateness only, which allows a control law based on electrochromic coating to be derived. Note that the perturbation due to J_2 is relevant throughout the whole LEO orbital range.

In a more simplified case when the only SRP effect is accounted for, from Eqs. (45) the secular rates of change of e and λ with respect to $\lambda_\odot$ become

$$\frac{\mathrm{d}e}{\mathrm{d}\lambda_\odot} = -\gamma\,\sin\lambda\,\sqrt{1-e^2} \quad , \quad \frac{\mathrm{d}\lambda}{\mathrm{d}\lambda_\odot} = -\gamma\,\cos\lambda\,\frac{\sqrt{1-e^2}}{e} - 1 \tag{47}$$

In this case the motion in the phase-space resembles that of a linear oscillator, starting from which a control strategy may be found to get for long-term stable areas in the orbital element phase-space. Among all sources of perturbations that have been neglected in Eqs. (47), the eclipses have a significant effect for low

and medium altitudes, because the working orbit belongs to the ecliptic plane. In particular, the eclipses squeeze the phase space in the direction of eccentricity and, for a given a, the equilibrium eccentricity decreases, and a precession of the apse line takes place [96]. The effects of eclipses may also be included in the SD dynamics. To that end, the Hamiltonian ($h = -\sqrt{1-e^2} + \alpha\, e \cos\lambda$) is first linearized. Then, the linearized equations are revised to account for a displacement in the center of rotation with respect to the equilibrium point. Finally, the effect of eclipses is introduced by replacing the analytical equilibrium eccentricity with the actual value, found numerically. Using such an approach, Lücking et al. have proposed a control algorithm, based on the electrochromic properties of the material, to achieve a steady value of the semimajor axis. The conclusion is that the reflectivity coefficient must be changed twice per orbit [96].

A suitable adjustment of the SD temperature, which results in a corresponding variation of the drag coefficient [64], is an interesting option for orbit control, and represents an alternative to an ECS in a geocentric case. For example, White et al. [64] have shown that the drag coefficient ranges from 2.15 to 2.2 when the SpaceChip temperature raises from 200 K to 405 K at an altitude of 600 km. This phenomenon is due to the radiometric forces, which arise when a thin plate with a thermal gradient between its two sides is surrounded by a rarefied gas [61, 62, 63]. These forces induce a displacement of the plate towards its cold side. Although the variation in the drag force acting on the device is small, it may have a non-negligible effect on the SD dynamics, due to the high area-to-mass ratio of the femtosatellite. Exploiting such a control strategy White et al. [64] estimated a maximum displacement per orbit of about 50 m at an altitude of 600 km. They also suggest that the relative position of a SpaceChips in a swarm may be maintained within prescribed limits.

6. Mission applications

The peculiar characteristics of SDs allow special and exotic mission scenarios to be feasible. The small size of SDs poses severe constraints on their payloads, which are usually sensors for space observations. The latter may offer interesting options for scientific missions or for diagnostic purposes. In the remainder of this section, some possible applications are presented, both for heliocentric and geocentric cases.

6.1. Heliocentric scenarios

Assuming $N = 1$ to simplify the analysis, Mengali and Quarta [78] discussed the variation of the SD orbital parameters as a function of the polar angle at which the ECSs are switched on (θ_{on}) and the angular interval $\Delta\theta$ within which they are kept in this "on" state. The results given by Eqs. (11), (13) and (14) show that, when the ECS is turned on for a whole revolution, the final value of the orbital eccentricity is fixed and independent of θ_{on}, whereas it depends on both θ_{on} and $\Delta\theta$ in a general case. However, the circularization of an elliptic parking orbit may be achieved only by a SD with a sufficiently large lightness number ($\beta \simeq 0.07$). The maximum value of the semimajor axis and the orbital eccentricity are both obtained when $\theta_{\text{on}} = 0$ and $\Delta\theta = \pi$, that is, by switching the ECS on at the perihelion and switching it off at the aphelion.

A simple mission case is to maximize the instantaneous time variation of the specific orbital energy (which amounts to maximizing the rate of change of the orbital semimajor axis), so as to perform an orbit raising and, eventually, insert the SD into an escape trajectory from the Solar System. In Ref. [78], it is found that, in order to maximize $\dot{a}$, the ECSs must be switched on ($\tau = 1$) when $\dot{r} > 0$ and off ($\tau = 0$) when $\dot{r} < 0$. This may be obtained by releasing the SD at the aphelion of the parking orbit and using working cycles with a constant period $\Delta\theta = \pi$. In this case, the final value of the Sun-SD distance r_{fin}, after N working cycles, is found with the following equation

$$r_{\text{fin}}(\theta) = \frac{p_0}{1 - \beta_{\min} - (e_0 - \beta_{\min} + 2\,N\,\Delta\beta)\,\cos\theta} \tag{48}$$

It is also possible to derive the minimum number of working cycles necessary to reach an escape conditions, given by

$$N_{\text{esc}} = \left\lceil \frac{1 - e_0}{2\,\Delta\beta} \right\rceil \tag{49}$$

where $\lceil \square \rceil$ is the ceil function.

The previous analysis of the relative motion of a SD with respect to a reference orbit enables the study of a second mission application, where the SD is used for diagnostic observations of another spacecraft, possibly

a MS from which the SD has been released. Mengali et al. [86] have studied the case of a MS placed on a reference (circular) orbit with radius r_c, which releases a SD with zero velocity relative to itself. The SD is required to perform a phasing maneuver and to come back to the MS orbit with a prescribed angular drift rate $\bar{\dot{\phi}}_{\rm des}$. To simplify the discussion, assume a single working cycle of the ECS (i.e., $N = 1$), and observe that Eq. (25) gives the time history of the state vector when the ECS is switched off, that is

$$\frac{\rho(t)}{r_c} = \beta_{\min}\,[1 - \cos(\Omega_c\,t)] + \Delta\beta[\cos(\Omega_c\,t - \Omega_c\,t_{\rm off}) - \cos(\Omega_c\,t - \Omega_c\,t_{\rm on})] \tag{50}$$

$$\phi(t) = \frac{2\,u_{\rm rel}(t)}{\Omega_c\,r_c} + 2\,\Delta\beta\,\Omega_c\,(t_{\rm on} - t_{\rm off}) - 2\,\beta_{\min}\,\Omega_c\,t \tag{51}$$

$$\frac{u_{\rm rel}(t)}{r_c} = \beta_{\min}\,\sin(\Omega_c\,t) + \Delta\beta\,[\sin(\Omega_c\,t - \Omega_c\,t_{\rm on}) - \sin(\Omega_c\,t - \Omega_c\,t_{\rm off})] \tag{52}$$

$$\frac{v_{\rm rel}(t)}{r_c} = -\frac{\rho(t)}{r_c} \tag{53}$$

The in-orbit repositioning maneuver is concluded in a time interval Δt when the SD comes back to touch the MS with zero velocity relative to it, that is $\rho(\Delta t) = 0$, $u_{\rm rel}(\Delta t) = 0$, $v_{\rm rel}(\Delta t) = 0$. Also, the mean angular drift rate must be equal to its design value, that is, $\phi(\Delta t)/\Delta t = \bar{\dot{\phi}}_{\rm des}$. Solving Eqs. (50)–(53) gives the following results for $t_{\rm on}$ and $t_{\rm off}$

$$t_{\rm on} = \frac{\Delta t}{2} - \frac{1}{\Omega_c}\,\arcsin\left[\frac{\beta_{\min}}{\Delta\beta}\,\sin\left(\frac{\Omega_c\,\Delta t}{2}\right)\right] \tag{54}$$

$$t_{\rm off} = \frac{\Delta t}{2} + \frac{1}{\Omega_c}\,\arcsin\left[\frac{\beta_{\min}}{\Delta\beta}\,\sin\left(\frac{\Omega_c\,\Delta t}{2}\right)\right] \tag{55}$$

$$\tag{56}$$

where the maneuver time Δt is found by numerically solving the equation

$$\sin\left(\frac{\bar{\dot{\phi}}_{\rm des} + 2\,\Omega_c\,\beta_{\min}}{4\,\Delta\beta}\,\Delta t\right) = \frac{\beta_{\min}}{\Delta\beta}\,\sin\left(\frac{\Omega_c\,\Delta t}{2}\right) \tag{57}$$

The limiting case occurs when the ECS is either always switched on or off. In the latter hypothesis, the angular drift for each MS revolution is given by Eq. (32), whereas if the ECS is always switched on, Eq. (32) can still be applied by substituting $\beta_{\min}$ with $\beta_{\max}$. The numerical results show that the angular drift rates are not very large, but still significant. If a small error is tolerable, for example $|\rho|/r_c \leq 3\%$ (see Eq. (30)), the mean time variation of the azimuthal coordinate is $\left|\bar{\dot{\phi}}\right| \leq 12\,\text{deg/year}$. Taking the extreme value $\bar{\dot{\phi}} = -12\,\text{deg/year}$, it is found that the ECS must be turned on at $t_{\rm on} \simeq 0.44\,T_c$ and switched off at $t_{\rm off} \simeq 0.83\,T_c$, where T_c is the orbital period of the MS. The corresponding total maneuver time is $\Delta t \simeq 1.27\,T_c$.

An interesting mission scenario for SDs involves the simultaneous use of a number of devices that form a Distributed Space System (DSS), as originally suggested by Shaw et al. [97]. Indeed, SDs offer a cheap option for remote sensing and scientific distributed space missions (DSMs) [16, 36, 37]. Barnhart et al. [36, 37] suggest to classify DSSs into two main groups: constellations and local clusters (or formations). In the first case, multiple satellites are suitably distributed in such a way as to execute the planned mission goals. When distributed in a local cluster, instead, the satellites form a swarm of objects, all of them flying in the same orbit, so as to perform a common target. While satellites in a constellation do not have stringent mutual orientation requirements, a formation flight requires a higher level of precision in the relative positioning and orientation among the satellites. The effectiveness of the DSM concept is that the risks are distributed in the cluster. Due to their small size and complexity, SDs seem more suited for a constellation arrangement, rather than for a local cluster. The dynamics of a swarm of SDs can be simulated by integrating the Eqs. (35)–(37).

6.2. Geocentric scenarios

A very promising geocentric mission application for SDs has been proposed by Colombo and McInnes [89, 90] and Zhao et al. [92], who discussed the equilibrium condition of femtosatellite orbits. Indeed, with the current technology level, the propulsive acceleration and the orbital perturbations could be exploited to guarantee a variation of the argument of perigee equal to the angular displacement of the Earth along its heliocentric orbit, while maintaining the semimajor axis and the orbital eccentricity both constant [89, 90, 92]. Starting from Eqs. (42), the conditions to be met are therefore

$$\Delta a_{\mathrm{SRP}} + \Delta a_{\mathrm{drag}} = 0 \quad , \quad \Delta e_{\mathrm{SRP}} + \Delta e_{\mathrm{drag}} = 0 \quad , \quad \Delta\omega_{\mathrm{SRP}} + \Delta\omega_{\mathrm{grav}} = \Delta\lambda_{\odot} = 2\pi\, n_{\oplus}\sqrt{a^3/\mu_{\oplus}} \tag{58}$$

of which the solutions, for orbits lying on the ecliptic plane, may be distinguished depending on the angle λ, see Fig. 12. In general, a solution to Eq. (58) does not exist. Hence, two families of partial equilibrium orbits are defined as

$$\Delta a = 0 \quad , \quad \Delta\omega = \Delta\lambda_{\odot} \tag{59}$$

or

$$\Delta e = 0 \quad , \quad \Delta\omega = \Delta\lambda_{\odot} \tag{60}$$

These two families both guarantee a Sun-synchronicity condition. Upon combining the solutions of Eqs. (59) and (60) it is possible to calculate the orbital parameters required for long-lived (quasi-stable) orbits. They are all characterized by two possible values of λ, that is, $\lambda = 0$ (when the orbit perigee is between the Earth and the Sun) or $\lambda = \pi$ (when the Earth is between the perigee and the Sun), see Fig. 12.

If $\lambda = 0$, the maximum eccentricity for a long-lived orbit is $e = 0.52$, while the maximum perigee altitude h_p is constrained by the value of A/m. In particular, for a given eccentricity, a larger value of A/m induces a smaller perigee altitude. If, instead, A/m is fixed and e is left free to vary, there exists a maximum value of h_p. Zhao et al. [92] have simulated this set of orbits along a time span of 30,000 revolutions with a spherical SD. Notably, h_p always stays below 3500 km and the eccentricity constraint is never violated. This considerations highlight that the solutions for $\lambda = 0$ are compatible with LEO scenarios and small orbital eccentricities, and are therefore useful for near-Earth applications, possibly using more than a single SD. Indeed, the previously described concept of DSSs has become attractive for many geocentric space applications [37], such as Earth imaging, detection and mapping of ionospheric plasma depletions [98, 99], and monitoring of drag environment [100]. Swarms of SDs may be used to collect spatially distributed data regarding the ionosphere and the exosphere, or for space weather, reflectometry, interferometry, and spectrometry purposes. Barnhart et al. have estimated that those advanced technologies may guarantee an order of magnitude of cost reduction when compared to current solutions [36]. Section 5 describes the approach proposed by Lücking et al. for orbital control, whose implementation allows swarms of SD devices to offer highly distributed sensing capability. Finally, the atmospheric drag may be exploited in the end-of-life conditions for the swarm re-entry phase, so as to mitigate the problem of space debris formation.

On the other hand, when $\lambda = \pi$, the perigee altitudes of long-lived orbits h_p are larger, and so are the eccentricities. In this case the numerical simulations discussed in Ref. [92] show that the perigee altitude h_p oscillates between the LEO and the HEO range, while the eccentricity e is always larger than 0.52. Therefore, this set of orbits could be useful for missions requiring the achievement of a larger geocentric distance. For example, a swarm of SDs could be conveniently used to increase the performance of GeoSail-type missions for analysis of the geomagnetic tail [101, 102].

7. Conclusions

The Smart Dust concept for space applications has been thoroughly discussed, starting from the basic architecture of a femtosatellite. A particular attention has been devoted to the analysis of Smart Dust dynamics under the effects of the gravitational pull, the propulsive acceleration due to solar radiation pressure, and other possible perturbation sources, with a methodological distinction between heliocentric and geocentric scenarios. Smart Dust satellites represent very-low-cost alternatives to more conventional configurations. They are able to substantially reduce a spacecraft mass by substituting the system with a single integrated circuit and to realize new operational missions, for example with monitoring purposes, for space weather applications, and in support of interplanetary exploration. Smart Dusts are especially attractive for

distributed science missions, since their architecture guarantees small costs, reasonable development efforts, system redundancy and fault tolerance. The discussion on possible mission applications has highlighted the enormous potentialities of this spacecraft concept. The technology level seems mature enough to enable the manufacturing of Smart Dusts with a good performance level, which is the necessary requirement for achieving ambitious scientific goals. In terms of operational missions, there is still a non-negligible gap between nano- and femto-spacecraft and larger and more expensive satellite projects. However, the miniaturization process is likely to be still further improved and the current technology level seems to be far from its theoretical limit. Besides the necessary technology advances, the future research should concentrate on solving the limitations in attitude control performance, especially in terms of dynamic control and control accuracies, which include the ECS design, as well as the yaw control problem with refractive prisms.

Acknowledgements

This work is supported by the University of Pisa, Progetti di Ricerca di Ateneo (Grant no. PRA_2018_44).

Conflict of interest statement

The authors declared that they have no conflicts of interest to this work.

References

[1] M. Rast, G. Schwehm, E. Attema, Payload-mass trends for earth-observation and space-exploration satellites, ESA bulletin 97 (1999) 73–77 .

[2] P. A. Dubock, F. Spoto, J. Simpson, D. Spencer, E. Schutte, H. Sontag, The Envisat satellite and its integration, ESA bulletin 106 (2001) 26–45 .

[3] M. N. Sweeting, M. Foquet, Earth observation using low cost micro/minisatellites, Acta Astronautica 39 (9–12) (1996) 823–826, doi: 10.1016/S0094-5765(97)00066-0.

[4] T. Wekerle, J. B. P. Filho, L. E. V. L. da Costa, L. G. Trabasso, Status and trends of smallsats and their launch vehicles - an up-to-date review, Journal of Aerospace Technology and Management 9 (3) (2017) 269–286, doi: 10.5028/jatm.v9i3.853.

[5] G. Laštovička-Medin, Nano/pico/femto-satellites: Review of challenges in space education and science integration towards disruptive technology, in: 5th Mediterranean Conference on Embedded Computing, MECO, Bar, Montenegro, 2016.

[6] S. Müncheberg, M. Krischke, N. Lemke, Nanosatellites and micro systems technology – capabilities, limitations and applications, Acta Astronautica 39 (9) (1996) 799–808, doi: 10.1016/S0094-5765(97)00063-5.

[7] R. J. Twiggs, Space system developments at Stanford University: From launch experience of microsatellites to the proposed future use of picosatellites, Proceedings of SPIE 4136 (2000) 79–86, doi: 10.1117/12.406646.

[8] F. Bruhn, J. Köhler, L. Stenmark, Nanospace-1: The impacts of the first Swedish nanosatellite on spacecraft architecture and design, Acta Astronautica 53 (4–10) (2003) 633–643, doi: 10.1016/S0094-5765(03)00109-7.

[9] A. Kestilä, T. Tikka, P. Peitso, et al., Aalto-1 nanosatellite - technical description and mission objectives, Geoscientific Instrumentation, Methods and Data Systems 2 (2013) 121–130, doi: 10.5194/gi-2-121-2013.

[10] S. Lätt, A. Slavinskis, E. Ilbis, et al., ESTCube-1 nanosatellite for electric solar wind sail in-orbit technology demonstration, Proceedings of the Estonian Academy of Sciences 63 (2S) (2014) 200–209, doi: 10.3176/proc.2014.2S.01.

[11] J. Praks, A. Kestilä, T. Tikka, H. Leppinen, O. Khurshid, M. Hallikainen, AALTO-1 Earth observation cubesat mission - education outcomes, in: International Geoscience and Remote Sensing Symposium (IGARSS), Milan, Italy, 2015.

[12] D. Gibbon, P. Charman, N. Kay, The design, development and in-orbit performance of a propulsion system for the SNAP-1 nanosatellite, in: 3rd International Conference on Spacecraft Propulsion, Cannes, France, 2000, pp. 91–98.

[13] C. I. Underwood, G. Richardson, J. Savignol, SNAP-1: A low cost modular COTS-based nano-satellite – design, construction, launch, and early operations phase, in: 15th Annual AIAA/USU Conference on Small Satellites, Logan, UT, USA, 2001.

[14] C. I. Underwood, G. Richardson, J. Savignol, In-orbit results from the SNAP-1 nanosatellite and its future potential, Philosophical Transactions of the Royal Society A: Mathematical, Physical and Engineering Sciences 361 (1802) (2003) 199–203, doi: 10.1098/rsta.2002.1123.

[15] J. Bouwmeester, J. Guo, Survey of worldwide pico- and nanosatellite missions, distributions and subsystem technology, Acta Astronautica 67 (7–8) (2010) 854–862, doi: 10.1016/j.actaastro.2010.06.004.

[16] T. Vladmirova, X. Wu, K. Sidibeh, Enabling technologies for distributed picosatellite missions in LEO, in: First NASA/ESA Conference on Adaptive Hardware and Systems, AHS 2006, Istanbul, Turkey, 2006, pp. 330–337.

[17] J. Puig-Suari, J. Schoos, C. Turner, T. Wagner, R. Connolly, R. Block, CubeSat development at Cal Poly: The standard deployer and Polysat, in: Small Payloads in Space, San Diego, CA, USA, 2000.

[18] I. Galysh, K. Doherty, J. McGuire, H. Heidt, D. Niemi, G. Dutchover, CubeSat: Developing a standard bus for picosatellites, Proceedings of SPIE 4136 (2000) 64–71, doi: 10.1117/12.406644.

[19] J. Shi, J. Costenbader, A COTS system solution for CCSDS spacecraft integration and test, in: IEEE Aerospace Conference, Snowmass at Aspen, CO, USA, 1999.

[20] D. Ngo, M. Harris, A reliable infrastructure based on COTS technology for affordable space application, in: IEEE Aerospace Conference, Vol. 5, Big Sky, MT, USA, 2001, pp. 52435–52442.
[21] D. Gibbon, M. Paul, L. Cowie, COTS (commercial off the shelf) propulsion equipment for low cost small spacecraft, in: 38th AIAA/ASME/SAE/ASEE Joint Propulsion Conference and Exhibit, Indianapolis, IN, USA, 2002.
[22] S. Waydo, D. Henry, M. Campbell, CubeSat design for LEO-based earth science missions, in: IEEE Aerospace Conference, Big Sky, MT, USA, 2002.
[23] R. Barza, Y. Aoki, K. Schilling, CubeSat UWE-1 - technology tests and in orbit results, in: AIAA 57th International Conference (IAC), Valencia, Spain, 2006.
[24] D. Selva, D. Krejci, A survey and assessment of the capabilities of CubeSats for Earth observation, Acta Astronautica 74 (2012) 50–68, doi: 10.1016/j.actaastro.2011.12.014.
[25] F. Nichele, S. Corpino, S. Seager, Three scenarios for valuable planetary science missions on Mars: Next generation of CubeSats to support space exploration, in: 65th International Astronautical Congress (IAC), Vol. 6, Toronto, ON, Canada, 2014, pp. 4121–4135.
[26] W. Su, J. Lin, T. Ha, Global communication coverage using CubeSats, in: 7th IEEE Annual Computing and Communication Workshop and Conference (CCWC), Las Vegas, NV, USA, 2017.
[27] A. Poghosyan, A. Golkar, CubeSat evolution: Analyzing CubeSat capabilities for conducting science missions, Progress in Aerospace Sciences 88 (2017) 59–83, doi: 10.1016/j.paerosci.2016.11.002.
[28] W. S. N. Trimmer, Microrobots and micromechanical systems, Sensors and Actuators 19 (3) (1989) 267–287, doi: 10.1016/0250-6874(89)87079-9.
[29] S. W. Janson, H. Helvajian, S. Amimoto, G. Smith, D. Mayer, S. Feuerstein, Microtechnology for space systems, in: IEEE Aerospace Applications Conference, Snowmass at Aspen, CO, USA, 1998, pp. 409–418.
[30] S. W. Janson, H. Helvajian, K. Breuer, MEMS, microengineering and aerospace systems, in: 30th Fluid Dynamics Conference, Norfolk, VA, USA, 1999.
[31] N. F. De Rooij, S. Gautsch, D. Briand, C. Marxer, G. Mileti, W. Noell, H. Shea, U. Staufer, B. Van Der Schoot, MEMS for space, in: TRANSDUCERS 2009 - 15th International Conference on Solid-State Sensors, Actuators and Microsystems, Denver, CO, USA, 2009, pp. 17–24.
[32] S. W. Janson, Mass-producible silicon spaecraft for 21st century missions, in: Space Technology Conference and Exposition, Reston, VA, USA, 1999.
[33] D. J. Barnhart, Satellite-on-a-chip: A feasibility study, in: Fifth Round Table on Micro/Nano Technologies for Space Workshop, Noordwijk, The Netherlands, 2005.
[34] D. J. Barnhart, T. Vladimirova, M. N. Sweeting, Satellite-on-a-chip feasibility for distributed space missions, in: CANEUS2006: Micro-Nano Technologies for Aerospace Applications, Toulouse, France, 2006.
[35] D. J. Barnhart, T. Vladimirova, M. N. Sweeting, System-on-a-chip design of self-powered wireless sensor nodes for hostile environments, in: IEEE Aerospace Conference, Big Sky, MT, USA, 2007.
[36] D. J. Barnhart, T. Vladimirova, M. N. Sweeting, Very-small-satellite design for distributed space missions, Journal of Spacecraft and Rockets 44 (6) (2007) 1294–1306, doi: 10.2514/1.28678.
[37] D. J. Barnhart, T. Vladimirova, A. M. Baker, et al., A low-cost femtosatellite to enable distributed space missions, Acta Astronautica 64 (11-12) (2009) 1123–1143, doi: 10.1016/j.actaastro.2009.01.025.
[38] J. Tristancho, J. Gutierrez-Cabello, A probe of concept for femto-satellites based on commercial-off-the-shelf, in: AIAA/IEEE Digital Avionics Systems Conference, Seattle, WA, USA, 2011, pp. 8A21–8A29.
[39] F. Y. Hadaegh, S. J. Chung, H. M. Manohara, On development of 100-gram-class spacecraft for swarm applications, IEEE Systems Journal 10 (2) (2016) 673–684, doi: 10.1109/JSYST.2014.2327972.
[40] A. Roman-Gonzalez, N. I. Vargas-Cuentas, Aerospace technology in Peru, in: International Astronautical Congress (IAC), Jerusalem, Israel, 2015, pp. 4292–4297.
[41] Z. Manchester, M. A. Peck, A. Filo, KickSat: A crowd-funded mission to demonstrate the world's smallest spacecraft, in: 27th Annual AIAA/USU Conference on Small Satellites, Logan, UT, USA, 2013.
[42] I. Kalnins, W. Bode, Aisat, Venta-1 and MaxValier nanosatellites based on quadsat platform, in: 62nd International Astronautical Congress 2011 (IAC 2011), Vol. 5, International Astronautical Federation, Curran Associates, Inc., New York, 2011, pp. 4130–4136.
[43] J. A. Atchison, M. A. Peck, Length scaling in spacecraft dynamics, Journal of Guidance, Control, and Dynamics 34 (1) (2011) 231–246, doi: 10.2514/1.49383.
[44] C. R. McInnes, Solar Sail: Technology, Dynamics and Mission Applications, Springer-Verlag, 1999, Ch. 2, pp. 32–55.
[45] A. A. Berlin, K. J. Gabriel, Distributed MEMS: New challenges for computation, in: IEEE computational science & engineering, Vol. 4, Xerox Corp, United States, 1997, pp. 12–16.
[46] J. M. Kahn, R. H. Katz, K. S. J. Pister, Next century challenges: mobile networking for "smart dust", in: 5th ACM/IEEE International Conference on Mobile and Computing Networks, Seattle, WA, USA, 1999, pp. 271–278.
[47] B. Warneke, M. Last, B. Liebowitz, K. S. J. Pister, Smart dust: Communicating with a cubic-millimeter computer, Computer 34 (1) (2001) 44–51, doi: 10.1109/2.895117.
[48] J. A. Atchison, M. A. Peck, A passive, sun-pointing, millimeter-scale solar sail, Acta Astronautica 67 (1–2) (2010) 108–121, doi: 10.1016/j.actaastro.2009.12.008.
[49] S. N. Kirpichnikov, E. S. Kirpichnikova, E. N. Polyakhova, A. S. Shmyrov, Planar heliocentric roto-translatory motion of a spacecraft with a solar sail of complex shape, Celestial Mechanics and Dynamical Astronomy 63 (3–4) (1995) 255–269, doi: 10.1007/BF00692290.
[50] J. A. Atchison, A passive microscale solar sail, in: Space 2008 Conference, San Diego, CA, USA, 2008.
[51] J. W. Wehner, C. M. Harris, M. K. O'Rell, Solar torque control using thin film directionally reflective, emissive, absorptive, and transmissive surfaces, United States Patent, Patent No. US6921050B2 (Jul. 26 2005).
[52] C. M. Harris, J. W. Wehner, Solar torque control by using thin-film directionally sensitive surfaces, in: AIAA Guidance, Navigation, and Control Conference, Honolulu, HI, USA, 2008.

[53] P. M. S. Monk, R. J. Mortimer, D. R. Rosseinsky, Electrochromism: Fundamentals and Applications, Wiley-VCH, 2007.
[54] C. Jack, C. S. Welch, Solar kites: small solar sail with no moving parts, Acta Astronautica 40 (2–8) (1997) 137–142, doi: 10.1016/S0094-5765(97)00120-3.
[55] B. Wie, Solar sail attitude control and dynamics, part 1, Journal of Guidance, Control, and Dynamics 27 (4) (2004) 526–535, doi: 10.2514/1.11134.
[56] G. Aliasi, G. Mengali, A. A. Quarta, Artificial Lagrange points for solar sail with electrochromic material panels, Journal of Guidance, Control, and Dynamics 36 (5) (2013) 1544–1550, doi: 10.2514/1.58167.
[57] J. Mu, S. Gong, J. Li, Coupled control reflectivity modulated solar sail for geosail formation flying, Journal of Guidance, Control, and Dynamics 38 (4) (2015) 740–751, doi: 10.2514/1.G000117.
[58] O. Mori, Y. Tsuda, Y. Shirasawa, T. Saiki, Y. Mimasu, J. Kawaguchi, Attitude control of IKAROS solar sail spacecraft and its flight results, in: 61st International Astronautical Congress, Prague, Czech Republic, 2010, paper IAC-10.C1.4.3.
[59] R. Funase, Y. Shirasawa, Y. Mimasu, O. Mori, Y. Tsuda, T. Saiki, J. Kawaguchi, On-orbit verification of fuel-free attitude control system for spinning solar sail utilizing solar radiation pressure, Advances in Space Research 48 (11) (2011) 1740–1746, doi: 10.1016/j.asr.2011.02.022.
[60] Y. Tsuda, O. Mori, R. Funase, H. Sawada, T. Yamamoto, S. Takanao, T. Endo, K. Yonekura, H. Hoshino, J. Kawaguchi, Achievement of IKAROS - Japanese deep space solar sail demonstration mission, in: 7th IAA Symposium on Realistic Advanced Scientific Space, Vol. 82, Aosta (Italy), 2011, pp. 183–188.
[61] N. P. Selden, C. Ngalande, N. E. Gimelshein, et al., Origins of radiometric forces on a circular vane with a temperature gradient, Journal of Fluid Mechanics 634 (2009) 419–431, doi: 10.1017/S0022112009007976.
[62] N. E. Gimelshein, S. F. Gimelshein, A. D. Ketsdever, et al., Shear force in radiometric flows, in: AIP Conference Proceedings, Vol. 1333, 2011, pp. 661–666.
[63] S. F. Gimelshein, N. E. Gimelshein, A. D. Ketsdever, et al., Analysis and applications of radiometric forces in rarefied gas flows, in: AIP Conference Proceedings, Vol. 1333, 2011, pp. 693–700.
[64] C. White, C. Colombo, T. J. Scanlon, Rarefied gas effects on the aerodynamics of high area-to-mass ratio spacecraft in orbit, Advances in Space Research 51 (11) (2013) 2112–2124, doi: 10.1016/j.asr.2013.01.002.
[65] A. B. Artusio-Glimpse, G. A. Swartzalder, Properties of oscillating refractive optical wings with one reflective surface, in: Optical Trapping and Optical Micromanipulation X, San Diego, CA, USA, 2013.
[66] S. Firuzi, S. Gong, Refractive sal and its applications in solar sailing, Aerospace Science and Technology 77 (2018) 362–372, doi: 10.1016/j.ast.2018.03.016.
[67] D. Ma, J. Murray, J. N. Munday, Controllable propulsion by light: Steering a solar sail via tunable radiation pressure, Advanced Optical Materials 5 (4) (2017) 1600668 (1–6), doi: 10.1002/adom.201600668.
[68] J. A. Burns, P. L. Lamy, S. Soter, Radiation forces on small particles in the Solar System, Icarus 40 (1) (1979) 1–48, doi: 10.1016/0019-1035(79)90050-2.
[69] A. Moro-Martin, R. Malhotra, Dynamical model of Kuiper belt dust in the inner and outer Solar System, The Astronomical Journal 125 (4 1768) (2003) 2255–2265, doi: 10.1086/368237.
[70] M. Harwit, Origins of the zodiacal dust cloud, Journal of Geophysical Research 68 (8) (1963) 2171–2180, doi: 10.1029/JZ068i008p02171.
[71] B. A. S. Gustafson, Physics of zodiacal dust, Annual Review of Earth and Planetary Sciences 22 (1994) 553–595, doi: 10.1016/0019-1035(79)90050-2.
[72] H. P. Robertson, H. N. Russel, Dynamical effects of radiation in the solar system, Monthly Notices of the Royal Astronomical Society 97 (6) (1937) 423–437, doi: 10.1093/mnras/97.6.423.
[73] J. Klačka, Solar wind dominance over the Poynting-Robertson effect in secular orbital evolution of dust particles, Monthly Notices of the Royal Astronomical Society 443 (1) (2014) 213–229, doi: 10.1093/mnras/stu1133.
[74] B. Dachwald, Minimum transfer times for nonperfectly reflecting solar sailcraft, Journal of Spacecraft and Rockets 41 (4) (2004) 693–695, doi: 10.2514/1.6279.
[75] A. F. Heaton, A. B. Artusio-Glimpse, An update to NASA reference sail thrust model, in: AIAA SPACE 2015 Conference and Exposition, Pasadena, CA, USA, 2015.
[76] G. Mengali, A. A. Quarta, Optimal three-dimensional interplanetary rendezvous using nonideal solar sail, Journal of Guidance, Control, and Dynamics 28 (1) (2005) 173–177, doi: 10.2514/1.8325.
[77] J. L. Wright, Space Sailing, Gordon and Breach Science Publishers, 1992, pp. 223–233.
[78] G. Mengali, A. A. Quarta, Heliocentric trajectory analysis of sun-pointing smart dust with electrochromic control, Advances in Space Research 57 (4) (2016) 991–1001, doi: 10.1016/j.asr.2015.12.017.
[79] C. R. McInnes, Azimuthal repositioning of payloads in heliocentric orbit using solar sails, Journal of Guidance, Control, and Dynamics 26 (4) (2003) 662–664, doi: 10.2514/2.5098.
[80] H. Yamakawa, Optimal radially accelerated interplanetary trajectories, Journal of Spacecraft and Rockets 43 (1) (2006) 116–120, doi: 10.2514/1.13317.
[81] A. A. Quarta, G. Mengali, Analysis of electric sail heliocentric motion under radial thrust, Journal of Guidance, Control, and Dynamics 39 (6) (2016) 1431–1435, doi: 10.2514/1.G001632.
[82] B. Dachwald, W. Seboldt, M. Macdonald, et al., Potential solar sail degradation effects on trajectory and attitude control, in: AIAA Guidance, Navigation, and Control Conference and Exhibit, San Francisco, CA, USA, 2005.
[83] B. Dachwald, G. Mengali, A. A. Quarta, M. Macdonald, Parametric model and optimal control of solar sails with optical degradation, Journal of Guidance, Control, and Dynamics 29 (5) (2006) 1170–178, doi: 10.2514/1.20313.
[84] B. Dachwald, M. Macdonald, C. R. McInnes, G. Mengali, A. A. Quarta, Impact of optical degradation on solar sail mission performance, Journal of Spacecraft and Rockets 44 (4) (2007) 740–749, doi: 10.2514/1.21432.
[85] C. R. McInnes, Approximate closed-form solution for solar sail spiral trajectories with sail degradation, Journal of Guidance, Control, and Dynamics 37 (6) (2014) 2053–2057, doi: 10.2514/1.G000225.
[86] G. Mengali, A. A. Quarta, E. Denti, Relative motion of sun-pointing smart dust in circular heliocentric orbits, Journal of Guidance, Control, and Dynamics 41 (4) (2018) 1009–1014, doi: 10.2514/1.G003088.

[87] C. R. McInnes, Simple analytic model of the long-term evolution of nanosatellite constellations, Journal of Guidance, Control, and Dynamics 23 (2) (2000) 332–338, doi: 10.2514/2.4527.
[88] C. R. McInnes, A continuum model for the orbit evolution of self-propelled 'smart dust' swarms, Celestial Mechanics and Dynamical Astronomy 126 (4) (2016) 501–517, doi: 10.1007/s10569-016-9707-y.
[89] C. Colombo, C. R. McInnes, Orbital dynamics of "smart-dust" devices with solar radiation pressure and drag, Journal of Guidance, Control, and Dynamics 34 (6) (2011) 1613–1631, doi: 10.2514/1.52140.
[90] C. Colombo, C. R. McInnes, Orbit design for future spacechip swarm missions in a planetary atmosphere, Acta Astronautica 75 (2012) 25–41, doi: 10.1016/j.actaastro.2012.01.004.
[91] C. Colombo, C. Lücking, C. R. McInnes, Orbit evolution, maintenance and disposal of spacechip swarms through electrochromic control, Acta Astronautica 82 (1) (2013) 25–37, doi: 10.1016/j.actaastro.2012.05.035.
[92] Y. Zhao, P. Gurfil, S. Zhang, Long-term orbital dynamics of smart dust, Journal of Spacecraft and Rockets 55 (1) (2018) 125–142, doi: 10.2514/1.A33854.
[93] D. P. Hamilton, A. V. Krivov, Circumplanetary dust dynamics: Effects of solar gravity, radiation pressure, planetary oblateness, and electromagnetism, Icarus 123 (2) (1996) 503–523, doi: 10.1006/icar.1996.0175.
[94] A. V. Krivov, J. Getino, Orbital evolution of high-altitude balloon satellites, Astronomy and Astrophysics 318 (1) (1997) 308–314 .
[95] C. Lücking, C. Colombo, C. R. McInnes, Orbit control of high area-to-mass ratio spacecraft using electrochromic coating, in: 61st International Astronautical Congress (IAC), Prague, Czech Republic, 2010, pp. 1923–1937.
[96] C. Lücking, C. Colombo, C. R. McInnes, Electrochromic orbit control for smart-dust devices, Journal of Guidance, Control, and Dynamics 35 (5) (2012) 1548–1558, doi: 10.2514/1.55488.
[97] G. B. Shaw, D. W. Miller, H. D. E., Generalized characteristics of communication, sensing, and navigation satellite systems, Journal of Spacecraft and Rockets 37 (6) (2000) 801–811, doi: 10.2514/2.3638.
[98] C. L. Enloe, L. Habash Krause, R. K. Haaland, et al., Miniaturized electrostatic analyzer manufactured using photolithographic etching, Review of Scientific Instruments 74 (3) (2003) 1192–1195, doi: 10.1063/1.1540715.
[99] L. Habash Krause, C. L. Enloe, R. K. Haaland, et al., Microsatellite missions to conduct midlatitude studies of equatorial ionospheric plasma bubbles, Advances in Space Research 36 (12) (2005) 2474–2479, doi: 10.1016/j.asr.2004.03.020.
[100] F. T. Hartley, Development and terrestrial applications of a nano-g accelerometer 3891 (1999) 410–415, doi: 10.1117/12.364471.
[101] C. R. McInnes, M. Macdonald, Geosail: Exploring the geomagnetic tail using a small solar sail, Journal of Spacecraft and Rockets 38 (4) (2001) 622–629, doi: 10.2514/2.3727.
[102] T. Oyama, H. Yamakawa, Y. Omura, Orbital dynamics of solar sails for geomagnetic tail exploration, Journal of Spacecraft and Rockets 45 (2) (2008) 316–323, doi: 10.2514/1.31274.